Journal of Materials Research and Technology 35 (2025) 2158–2175

Contents lists available at ScienceDirect

Journal of Materials Research and Technology

journal homepage: www.elsevier.com/locate/jmrt

Research on the optimization of mechanical properties of triply periodic minimal surfaces in composite materials prepared with the assistance of acoustic fields

Shuai Guo [a,c,*], Xianliang Sheng [b], Anfu Guo [b,**], Wenlu Yang [b], Xiaolin Zhao [a], Shang Sui [d,e], Jiaqiang Li [f,g], Yufan Zhao [c,h], Meng Wang [c,h], Xin Lin [c,h]

[a] *School of Materials Science and Engineering, Liaocheng University, Liaocheng, Shandong, 252000, People's Republic of China*
[b] *School of Mechanical and Automotive Engineering, Liaocheng University, Liaocheng, Shandong, 252000, People's Republic of China*
[c] *MIIT Key Laboratory of Metal High Performance Additive Manufacturing and Innovative Design, Northwestern Polytechnical University, Xi'an, Shaanxi, 710072, People's Republic of China*
[d] *School of Materials Science and Engineering, Xi'an University of Technology, Xi'an, Shaanxi, 710048, People's Republic of China*
[e] *Xi'an Key Laboratory of Advanced Magnesium Alloy Additive Manufacturing and Precision Forming, Xi'an, Shaanxi, 710048, People's Republic of China*
[f] *School of Mechanical and Electric Engineering, Soochow University, 8 Jixue Road, Suzhou, 215000, People's Republic of China*
[g] *Advanced Manufacturing Technology Research Center, Department of Industrial and Systems Engineering, The Hong Kong Polytechnic University, Kowloon, Hong Kong*
[h] *State Key Laboratory of Solidification Processing, Northwestern Polytechnical University, Xi'an, Shaanxi, 710072, People's Republic of China*

ARTICLE INFO

Handling editor: Prof. M Meyers

Keywords:
Laser powder bed fusion
Composite material
Functionally graded
Energy absorption
Acoustic fields

ABSTRACT

Lattice structures have garnered significant attention due to their superior mechanical properties. However, while maintaining the lightweight advantages of lattice structures, further enhancing their strength is of paramount research significance. This paper proposes an optimized Gyroid Sin Square (GSS) gradient structure and fabricates composite materials and epoxy interpenetrating phase composites (IPCs) lattice structures using Laser Powder Bed Fusion (LPBF) combined with Acoustic Fields (AF). The mechanical characteristics were examined through uniaxial compression experiments. The findings suggest that the composite lattice shows remarkably greater specific energy absorption (SEA) in contrast to the initial lattice. With the introduction of AF, the z-axis gradient 5 wt% tungsten carbide (WC) composite GSS structure exhibited a 76.78% improvement in SEA compared to the uniform original structure. The IPCs demonstrated the highest plateau stress, which can be attributed to the physical interlocking between the epoxy resin and the substrate, effectively enhancing deformation resistance. However, due to the earlier densification of IPCs during loading, SEA is somewhat reduced compared to the composite structures. The addition of WC led to grain refinement and weakened the texture. Meanwhile, the acoustic streaming and cavitation effects generated by the AF reduced residual stress, ultimately improving the overall mechanical properties of the lattice structures.

1. Introduction

Lattice structures, characterized by high strength, high specific surface area, excellent thermal insulation, and energy absorption capabilities [1–3], find extensive use in multiple fields like defense, auto manufacturing, and medicine [4–6]. Typical lightweight lattice structures, such as honeycombs [7], and truss structures [8], although possessing significant advantages, often suffer from mechanical instability due to stress concentration at the nodes, limiting further performance enhancement. Therefore, the development of lattice structures with excellent mechanical properties is crucial to meet complex engineering demands. The fabrication of controllable lattices with internal structures has been made possible by the application of additive manufacturing technologies [9,10]. Laser powder bed fusion (LPBF) allows for the layer-by-layer scanning of metal powder beds, achieving metallurgical bonding through melting and solidification, thus producing high-precision porous metal parts [11].

As lattice structures are becoming more common in engineering

---

* Corresponding author. School of Materials Science and Engineering, Liaocheng University, Liaocheng, Shandong, 252000, People's Republic of China.
** Corresponding author.
E-mail addresses: shuaiguo@lcu.edu.cn (S. Guo), guoanfu@lcu.edu.cn (A. Guo).

https://doi.org/10.1016/j.jmrt.2025.01.191
Received 22 December 2024; Received in revised form 17 January 2025; Accepted 24 January 2025

applications, improving their energy absorption performance has become a key research focus. In recent years, inspired by natural structures, triply periodic minimal surface (TPMS) have garnered significant attention due to their periodic variation in three-dimensional space, zero mean curvature, high porosity, and continuous surface curvature characteristics, which effectively mitigate stress concentration [12,13]. Yang et al. [14] conducted an in-depth study on the compressive fatigue behavior of Gyroid structure and found that the specimen fractured at 45° along the diagonal under the fatigue loading stress, while sandblasting could improve the fatigue resistance of the specimen. Jin et al. [15] analyzed the effect of staggered Gyroid lattice units on the mechanical properties of Ni–Ti, and the results showed that at the same volume fraction with the results show that with the increase of interlaced units at the same volume fraction the stress distribution of the lattice structure is more uniform, and the improved lattice structure has excellent superelasticity. Zhang et al. [16] studied TPMS structures and traditional body-centered cubic (BCC) structures made from 316L stainless steel (316L SS) using LPBF and found TPMS to outperform BCC lattices in various performance metrics. However, biological materials in nature, such as wood, pomelo peel, and bones, commonly exhibit hierarchical structures [12,17,18]. Inspired by these natural examples, functional gradient (FG) TPMS structures, which adjust pore distribution by varying structural parameters, have provided new avenues for optimizing structural performance [19].Wu et al. [20] investigated the mechanical response of homogeneous and gradient lattices of SiC prepared by LPBF and found that gradient lattices have superior fatigue properties and deformation resistance. Yang et al. [21] examined the mechanical properties of Gyroid lattices made from LPBF 316L SS, demonstrating that gradient structures gradually increase their load-bearing capacity during compression and exhibit superior energy absorption performance compared to uniform structures. Further studies by Zhang et al. [22] and Wang et al. [23] have revealed the impact of geometry and size on the mechanical behavior of TPMS lattices, as well as the enhancing effects of continuous interface design in FG lattice structures on deformation stability and load-bearing capacity.

It is noteworthy that the mechanical characteristics of lattice structures are influenced by factors such as cell type and volume fraction (ρ*) [24,25]. Currently, methods to optimize the lattice structures primarily include changing cell types and increasing relative density, but these approaches often lead to reduced porosity, thereby sacrificing the lightweight advantages of the structure. To enhance mechanical performance without compromising the lightweight benefits, 3D-printed TPMS lattice structures can be reinforced with a secondary phase material. This approach combines the optimal features of solid components to meet specific functional and mechanical requirements [26]. For example, Luo et al. [27] designed heterogeneous honeycomb sandwich structures using a combination of topology and material reinforcement, finding that the reinforced heterogeneous honeycomb sandwich structures exhibited significantly improved compressive strength and elastic modulus. Zhang et al. [28] studied in situ fabricated TiB/Ti6Al4V gradient material Gyroid specimens, and the results showed that the stiffness and strength of the gradient material structure were better than the original structure. Furthermore, Guo et al. [29] proposed an anisotropic heterogeneous scaffold design that simulates natural materials, discovering that the improved scaffold model significantly enhanced energy absorption performance.

However, the design flexibility of single lattice structures is relatively limited and sometimes insufficient to meet specific engineering requirements [30]. To address this issue, filling lattices with secondary materials has emerged as an effective composite design method. Designing interpenetrating phase composites (IPCs) topologies using matrix and filler materials as design variables greatly increases design flexibility. Guo et al. [31] conducted an in-depth study on hollow P-lattices and their IPCs P-lattices, showing that the optimized P-lattices exhibited superior strength and specific energy absorption (SEA) compared to the original P-lattices. Jhaver et al. [32] prepared IPCs by permeating epoxy composite foam into open-cell aluminum foam and found that the energy absorption was 50% higher than that of unfilled samples. Duarte et al. [33] investigated the compressive performance and energy absorption capabilities of open-cell aluminum foams filled with different materials (such as polymers, epoxy resin (EP), and silicone rubber). The results indicated that samples filled with EP had higher compressive strength and energy absorption capabilities. Li et al. [34] developed novel metal lattice-epoxy composites, which demonstrated excellent strength enhancement effects.

The microstructure also significantly affects the mechanical properties of lattice structures [35,36]. Notably, the large thermal gradient in the LPBF process generates residual stresses, which may lead to defects such as cracks and porosity, ultimately compromising mechanical performance. To address these issues, some researchers have proposed that the cavitation and acoustic streaming effects induced by Acoustic Fields (AF) can enhance melt pool flow, reduce residual stress, and increase material densification, thereby optimizing the mechanical properties of materials [37,38]. For example, Ning et al. [39]examined the impact of AF on 17-4 PH steel manufactured by DED. The findings indicated that with the addition of AF, the porosity was reduced from 0.68% to 0.35%. Wang et al. [40] investigated the impact of AF-assisted DED on the mechanical properties and microstructure of Inconel 718 alloys, revealing that AF significantly refined the grain size of the alloy. Tilita et al. [41] applied AF to the LPBF process and found that AF reduced the anisotropy of 304L stainless steel. Therefore, introducing AF into the LPBF process is an effective method for enhancing mechanical performance.

Building on the above research, this study combines the advantages of composite materials and EP to propose an internal and external reinforcement method aimed at optimizing the mechanical properties of TPMS structures. By introducing AF and incorporating second-phase ceramic particles to reinforce 316L SS and using EP as a filling material, we designed IPCs lattice structures to enhance strength while maintaining lightweight characteristics. Uniform and gradient Gyroid TPMS lattices along the z-axis and x-axis were fabricated using LPBF technology, and their surface morphology was analyzed using scanning electron microscope (SEM). Subsequently, uniaxial compression tests were conducted to analyze the deformation mechanisms, mechanical characteristics of different gradient TPMS lattices. Finite element analysis was also employed to study the stress-strain distribution.

2. Material and method

2.1. Design of the structure

The Gyroid structure can be generated utilizing implicit equations [42], which generate a three-dimensional surface as the solution of a level set function Φ, described as follows:

$$\Phi_G(x,y,z) = \cos(\omega x)\sin(\omega y) + \cos(\omega y)\sin(\omega z) + \cos(\omega z)\sin(\omega x) - t \quad (1)$$

where x, y, z are coordinates, $\omega = 2\pi/l$, l is the unit cell length.

The gradient variation in TPMS can be altered using different gradient control functions. Using Flatt Pack software [42] to model the Gyroid structure, the control function of the Gyroid structure is established (Eq. (1)), and the gradient distribution is modified by adjusting the position function $t(x,y,z)$. The ρ* of the lattice structure is expressed as the ratio of the volume of material in the lattice structure to the total volume [43]. By establishing the relationship between the ρ* and the sine function (Eq. (2)) and the sine squared function (Eq. (3)) along the z-axis, nonlinear gradient lattice structures can be obtained.

$$\rho^*_{sin}(z) = 0.3 + 0.1\, sin\,(2\pi z) \quad (2)$$

$$\rho^*_{\text{sin square}}(z) = 0.2 + 0.2\, sin^2\,(2\pi z) \quad (3)$$

According to previous studies [44,45], the mechanical properties of the lattice structure can be reliably evaluated by using a $5 \times 5 \times 5$ lattice arrangement when boundary effects are considered. In this study, Gyroid structures with unit cell dimensions of 4 mm, $5 \times 5 \times 5$ arrays were designed. Since total weight is a critical attribute of lattice structures, comparisons between different configurations are only meaningful if the mass is the same. Therefore, in this study, ρ^* is designed to be 30% lattice structure as shown in Fig. 1 (a). As per Eq. (1), Eq. (2), and Eq. (3), the Z-axis gradient change of the Gyroid sin (GSz) and the Gyroid sin square (GSSz)structure can be obtained. Fig. 1 (c) illustrates the methodology for generating these two Gyroid structures,

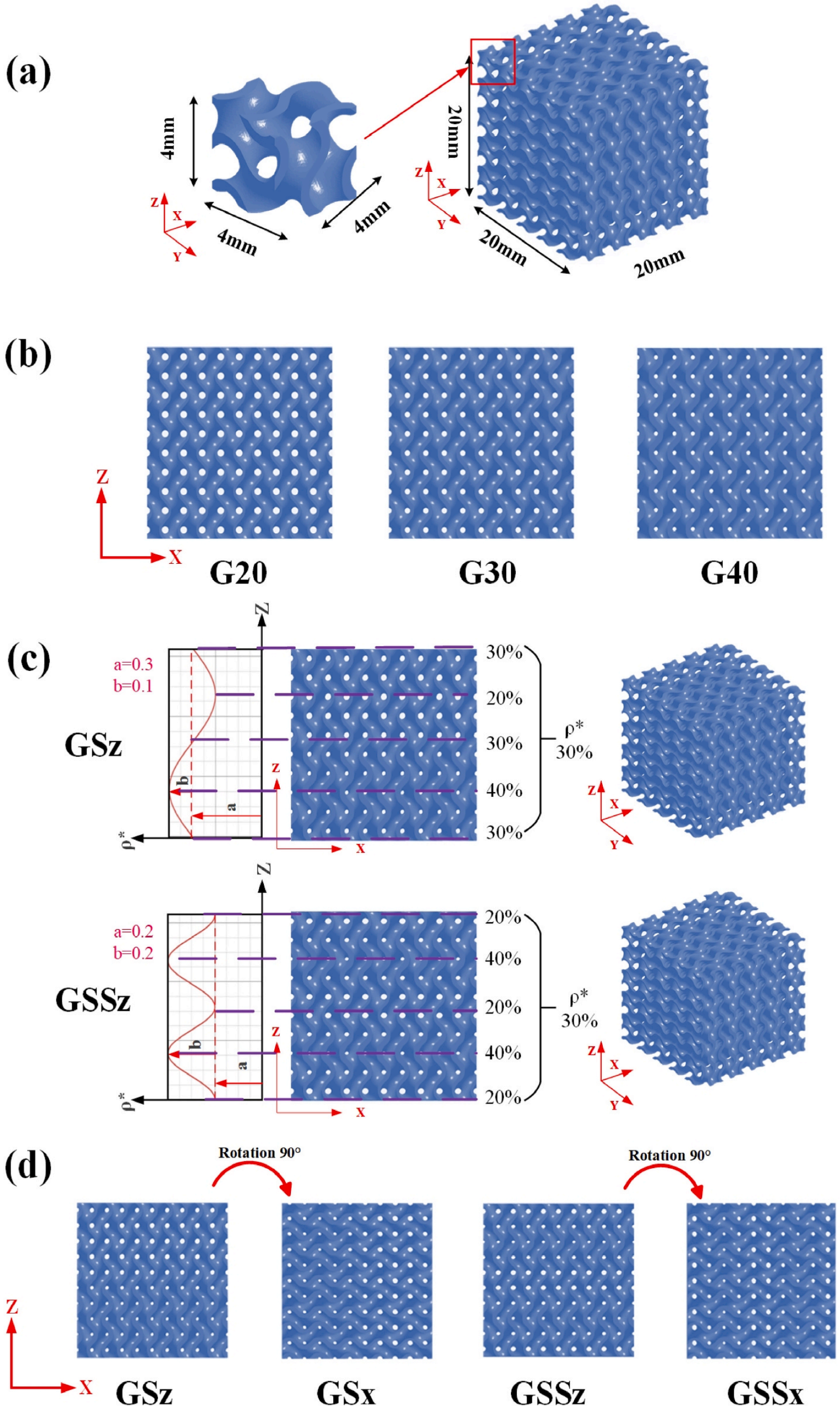

Fig. 1. Gyroid structure modeling methodology: (a) CAD (Computer Aided Design) representation of Gyroid unit cell; (b) CAD representation of Gyroid structures with ρ^* of 20%, 30% and 40%; (c) lattice structure design curves and CAD structural modeling along the build-up direction; (d) Gyroid structure with gradient direction perpendicular to the z-axis.

where 'a' represents the baseline ρ*, and 'b' represents the amplitude. In Fig. 1 (d), the Gyroid structure is rotated 90° relative to the Y-axis and denoted as GSx and GSSx to study the anisotropy of mechanical properties. For reference, uniform structures with ρ* of 20%, 30%, and 40% (G20, G30, G40) were also fabricated, as shown in Fig. 1 (b). In this paper, the gradient is defined as Gz for samples along the z-axis and Gx for samples perpendicular to the z-axis.

2.2. Materials and manufacturing

Composite materials were prepared using 3–5 μm tungsten carbide (WC) powder and 15–53 μm gas-atomized 316L SS powder. According to the ball milling parameters from previous studies [11], the planetary ball mill was used to mix WC and 316L SS powder, with the ball milling process depicted in Fig. 2 (a). Fig. 2 (b) shows the particle size distribution of 316L SS. Fig. 2 (c, d) shows the powder morphology observed by SEM. The powders exhibited good sphericity and uniform particle size distribution, with WC uniformly attached to the 316L SS powder.

Single-material and composite Gyroid structures were fabricated using an LPBF machine (FS121 M, Farsoon Technologies Co., LTD, China), with the processing parameters shown in Table 1. Fig. 3 (a) illustrates the schematic of the AF-assisted LPBF process. It is important to note that the acoustic field generator is installed at the angle above the LPBF machine and composed of a power supply, diaphragm, permanent magnet, power amplifier, and other auxiliary components. The acoustic waves, along with accompanying mechanical vibrations, interact with the melt pool, transmitting energy at a frequency of approximately 2000 Hz. This design aims to efficiently deliver energy to the melt pool in a non-contact manner, enabling the achievement of specific process objectives. To reduce residual stress during processing, the laser was rotated 67° for each layer alternately (Fig. 3 (b)). The printing process was carried out in an argon atmosphere (Fig. 3 (c)). The prepared samples are shown in Fig. 3 (d).

Table 1
LPBF processing parameters.

Laser power	Layer thickness	Scanning speed	Hatch spacing	Oxygen content
200 W	30 μm	1000 mm/s	70 μm	<0.1%

The specific types of samples prepared were as follows: specimens prepared with 316L SS alone (GSz-AS, GSSz-AS, GSx-AS, GSSx-AS), specimens prepared with 3 wt% WC composites (GSz-3% WC, GSSz-3% WC, GSx-3% WC, GSSx-3% WC), specimens prepared with 5 wt% WC composites (GSz-5% WC, GSSz-5% WC, GSx-5% WC, GSSx-5% WC), specimens of 5 wt% WC composites with AF (GSz-5% WC-AF, GSSz-5% WC-AF, GSx-5% WC-AF, GSSx-5% WC-AF), and specimens of 5 wt% WC composites with AF and coated with EP (GSz-5%WC-AF-EP, GSSz-5% WC-AF-EP, GSx-5%WC-AF-EP, and GSSx-5%WC-AF-EP). The coating agent preparation process is detailed in the Supplementary Material, and its main quality indicators are shown in Table S1 of the Supplementary Material.

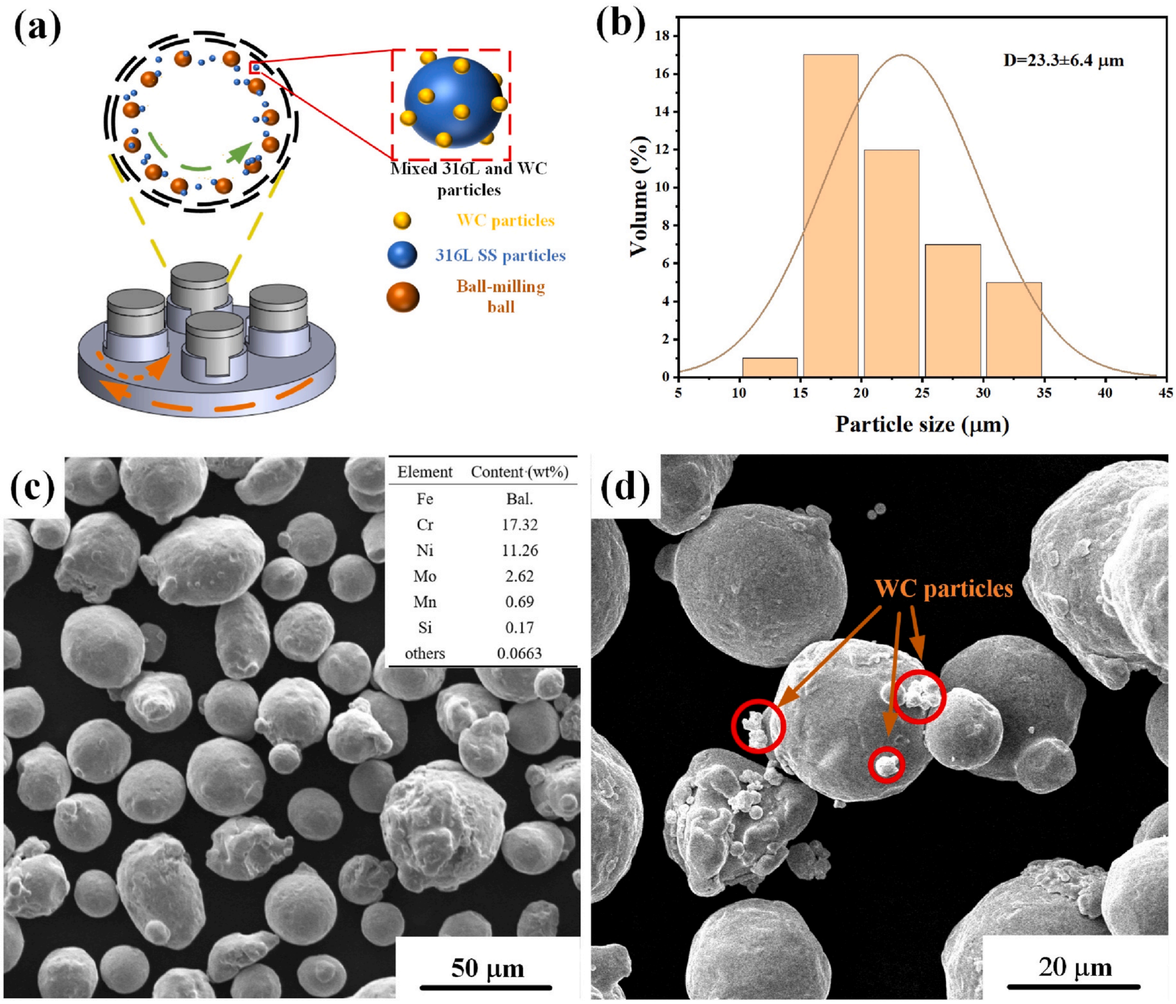

Element	Content (wt%)
Fe	Bal.
Cr	17.32
Ni	11.26
Mo	2.62
Mn	0.69
Si	0.17
others	0.0663

Fig. 2. SEM images showing morphologies of schematic diagram of ball milling principle (a), 316L SS particle size distribution (b), 316L SS particles (c), and WC/316L SS particles (d).

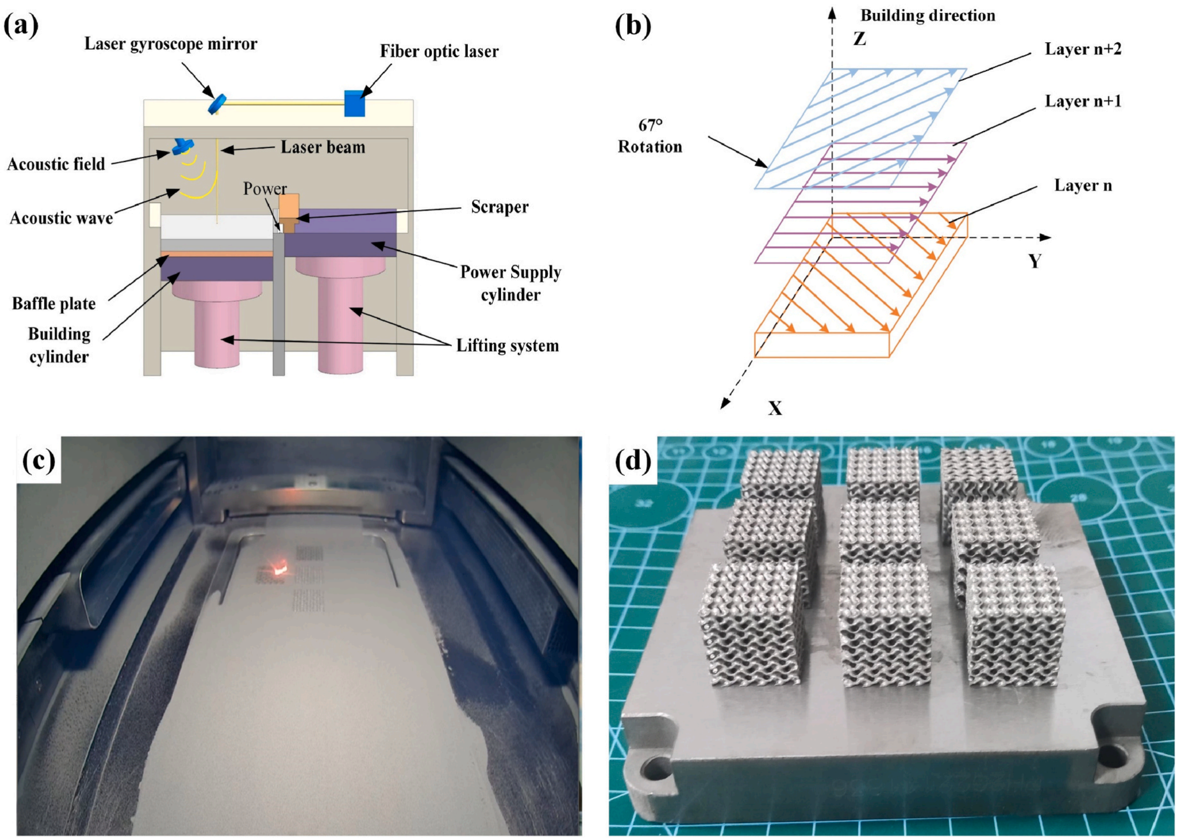

Fig. 3. (a) Principle of the equipment; (b) Rotation 67° scanning strategy; (c) LPBF process; (d) As-built samples.

The configured impregnation agent was used to coat the TPMS samples, forming a thin layer on their surfaces. To ensure the impregnation agent had a sufficiently low viscosity and could fully contact the part surfaces while preventing the resin from curing at high temperatures, an infiltration temperature of 80 °C was selected. To ensure an even coating, the samples were coated under negative pressure (−90 kPa) at 80 °C for 30 min in a vacuum drying oven. Finally, all samples were cured in a 125 °C oven for 3 h and cooled to room temperature. The detailed process is illustrated in Fig. 4.

2.3. Measurements and characterization

The quasi-static compression test was conducted by WDW-300 testing machine with a test speed of 1 mm/min, as shown in Fig. 5 (a). To ensure consistency in the effect of print direction on material properties, all samples were loaded in the same direction as the print direction. Tests were terminated when the samples reached 75% strain or the load limit, with a camera recording the entire compression process. According to ISO 13314 [46], the elastic modulus (E) was defined

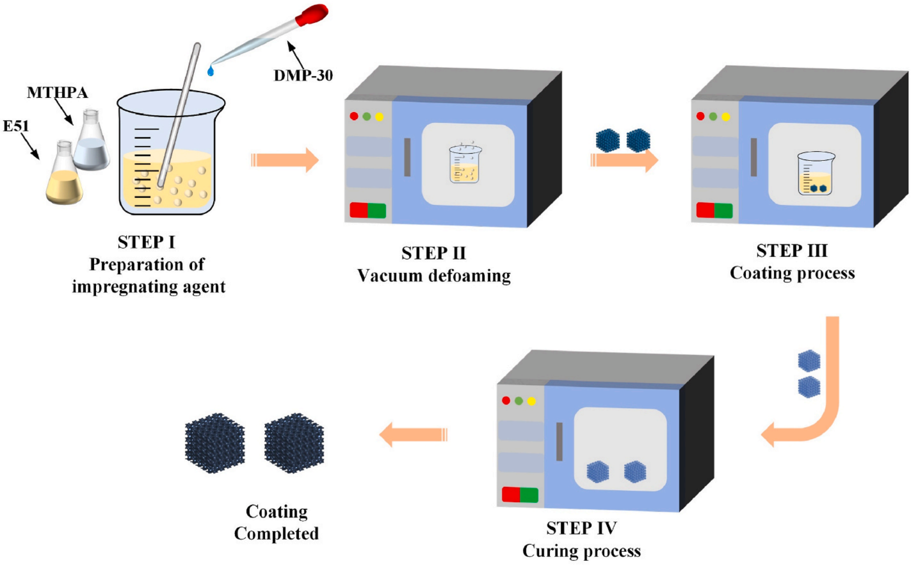

Fig. 4. Diagram of impregnation coating process of impregnating agent.

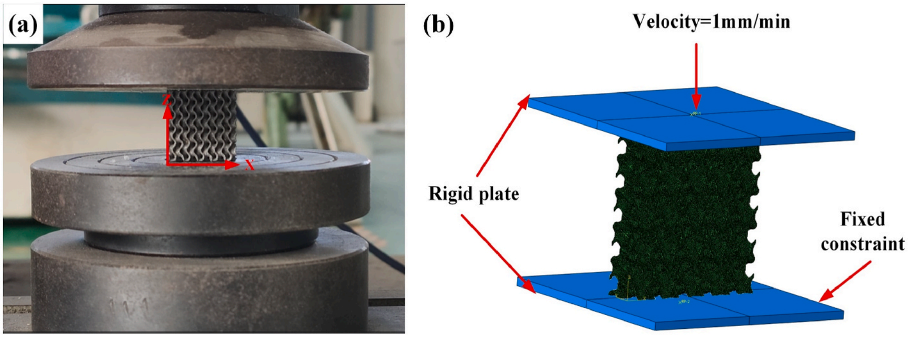

Fig. 5. (a) Compression test procedure; (b) FEA model.

as the slope of the linear portion of the stress-strain curve, and the yield strength (σ_y) was defined as the 0.2% offset relative to E. The plateau stress (σ_{pl}) was calculated as the arithmetic mean of the stress in the 0.2–0.4 compression strain range.

To observe the microstructure, the TPMS samples were first polished with SiC sandpaper up to 2000 grit, followed by polishing with a 1 μm diamond suspension, and finally chemically etched for 15 s using aqua regia (75% HCl, 25% HNO_3). X-ray diffraction (XRD) was used to analyze the phase composition, with a scanning speed of 5°/min over a range of 5~90°. A scanning electron microscope (GX4, Thermo Fisher, Waltham, Massachusetts, USA), which is equipped with an energy spectrometer (EDS), was employed to observe the surface morphology and elemental distribution of the samples. Electron backscatter diffraction (EBSD, Oxford Nordlys max3) was used to analyze the microstructural features of the samples. The scanning speed was 1 μm/s, and the test area was 1000 × 1000 μm^2.

2.4. *Finite element analysis*

The stress-strain behavior of the Gyroid structure was simulated using Abaqus software. To reduce computational costs and visually display the stress distribution, a 5 × 1 × 5 model was selected for finite element analysis, which is widely accepted in the literature [47]. The Gyroid model is generated based on the voxel mesh as shown in Fig. 5 (b). Two rigid plates were used to simulate the boundary conditions of the compression process, and the friction coefficient was set to 0.2. The bottom plate was fixed, while the top plate moved downward under a displacement load at the same speed as the experiment (1 mm/min).

3. Results and discussion

3.1. *Surface topography*

Fig. 6 illustrates the surface morphology of the samples observed by SEM. The geometrical features of the sample are clear and no defects such as cracks and warps caused by 3D printing were found. The surface of the structure shows incompletely melted powder particles due to the layer-by-layer build process. Fig. 6 (a, b) show the upper surface morphology of the samples, and the stepped structure is a result of uneven thermal shrinkage of the preceding layer during each printing cycle. Additionally, the top surface exhibits a small amount of unmelted powder due to incomplete melting and solidification processes. Fig. 6 (c, d) display the side surface morphology of the samples. When printing complex surfaces without supports, loose metal powder fails to effectively support the solidified metal particles at horizontal interfaces, resulting in localized adhesion of metal powder and a rougher side surface compared to the top. This phenomenon is attributed to differences in thermal diffusion coefficients between unmelted and melted powders, as well as the enlargement and partial sinking of the melt pool into the underlying powder layers [48].

For complex structures, besides deviations caused by the enlargement of melt pools and powder adhesion, the overhanging phenomenon is also an important factor for localized deviations [49]. The formation of unmelted particles and overhanging structures on support plate surfaces is attributed to a combination of factors including low angles of support plates, the thermal influence zone of the laser beam, and the inherent characteristics of LPBF manufacturing. These factors can lead to geometric deviations between the designed and manufactured samples.

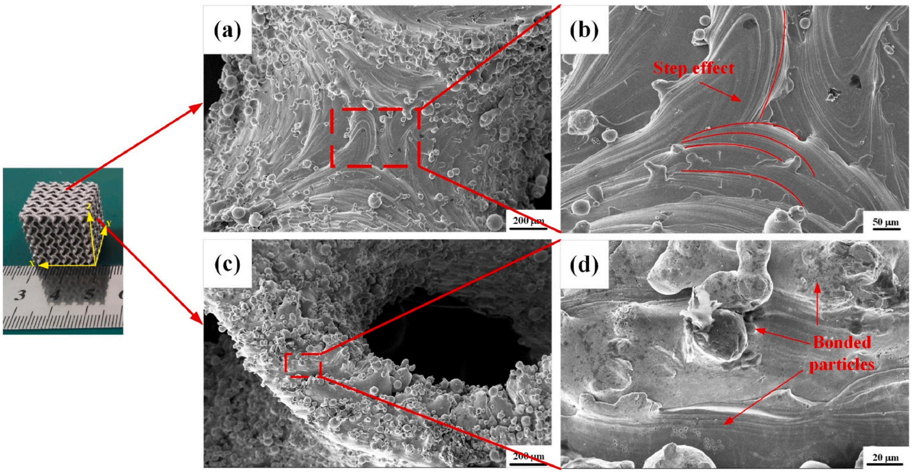

Fig. 6. SEM images of TPMS lattice surfaces: (a) top surface; (b) localized magnification with respect to (a); (c) side surface; (d) localized magnification with respect to (c).

3.2. Compression curves and mechanical properties

3.2.1. Stress-strain curve

The stress-strain curves of uniform and gradient structures are shown in Fig. S1 and Fig. 7, respectively. In Fig. S1, it can be observed that the stress-strain curves of uniform structures exhibit similar trends, characterized by three distinct stages: initially, a linear elastic deformation stage; followed by an elastic-plastic deformation stage where significant energy is absorbed; and finally, entering a stage of rapid stress increase indicative of densification. These stages are detailed in Section 3.5 (Fig. 16). Fig. 7 demonstrates that samples with different WC contents within the same gradient structure exhibit similar stress-strain trends. For the Gz structure, the load-carrying capacity gradually increases during compression, with the stress-strain curve showing a distinct upward trend. This is attributed to increased contact between the higher porosity regions after deformation, providing effective support to the remaining parts and thus enhancing post-failure load-carrying capacity. In contrast, for the Gx structure, where the ρ* distribution in the y-z plane remains uniform during loading, similar to the uniform structure, the stress-strain curve exhibits a longer yield plateau after the elastic stage. The gradient variation is the primary reason for the differences observed in these curve trends.

On the other hand, the compression stress-strain curves of structures prepared with composite materials and AF are higher than those prepared with 316L SS alone, due to the increased stiffness imparted by the composite materials. It is noteworthy that, influenced by both material properties and structural factors, early contact between adjacent layers weakens the stress variation between layers, resulting in compression stress-strain curves without significant stress fluctuations. During the compression process, all structures exhibited continuous hardening behavior without noticeable strength loss or pronounced peak stress, which is a significant characteristic of sheet TPMS structures.

3.2.2. Mechanical properties

The mechanical performance of uniform TPMS structures is shown in Fig. S2. It can be observed that the mechanical properties of the uniform structures significantly improve with increasing ρ*. As the ρ* increases from 20% to 40%, the elastic modulus increases from 1085.33 MPa to 2565.67 MPa, the plateau stress increases from 44.73 MPa to 157.20 MPa, and the yield strength increases from 29.09 MPa to 91.77 MPa.

The compressive properties of the samples derived from Fig. 7 are shown in Fig. 8. Fig. 8 demonstrates that the mechanical properties of the Gyroid structures are influenced by gradient distribution, relative density distribution, and material composition. Due to the reinforcing effect of WC, the mechanical performance of the Gyroid structures is significantly enhanced. The structures with 5% WC reinforced by AF and coated with EP exhibit superior mechanical performance compared to those fabricated with single materials. Specifically, GSSx-5% WC-AF-EP shows the highest elastic modulus at 2392 MPa, which is 24.77% higher than the GSSx sample and 44.49% higher than the G30 sample. The plateau stress of GSSx-5%WC-AF-EP reaches 152.33 MPa, which was 52.97% higher than that of the original sample and 59.74% higher than that of the homogeneous sample. The reasons for these strength improvements will be detailed in Section 3.4.

In low-strain conditions, the Gz-type samples exhibit initial yielding deformation in regions with higher porosity, with the elastic modulus primarily determined by the performance of the thinner layers. In contrast, the Gx samples demonstrate excellent elastoplastic

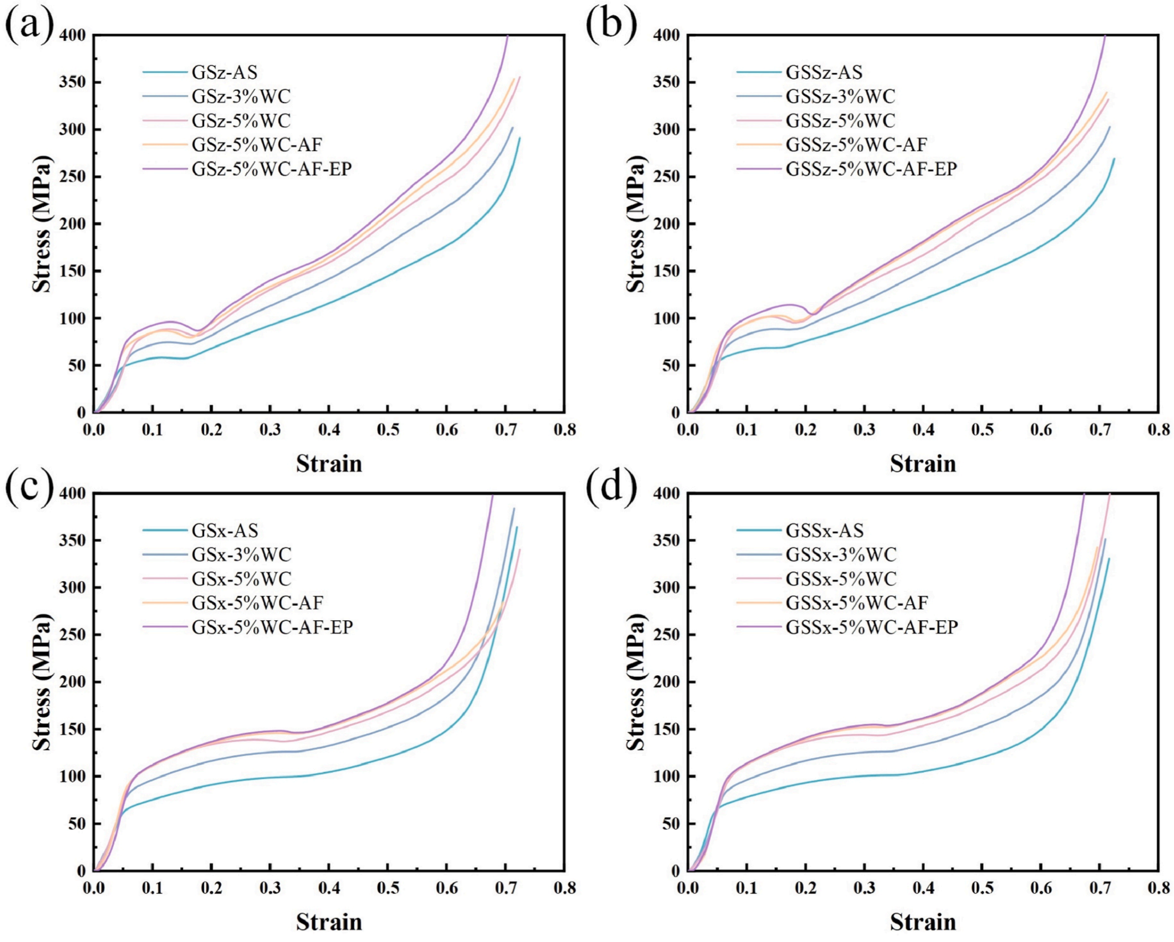

Fig. 7. The compression curve of (a) GSz; (b) GSSz; (c) GSx; (d) GSSx.

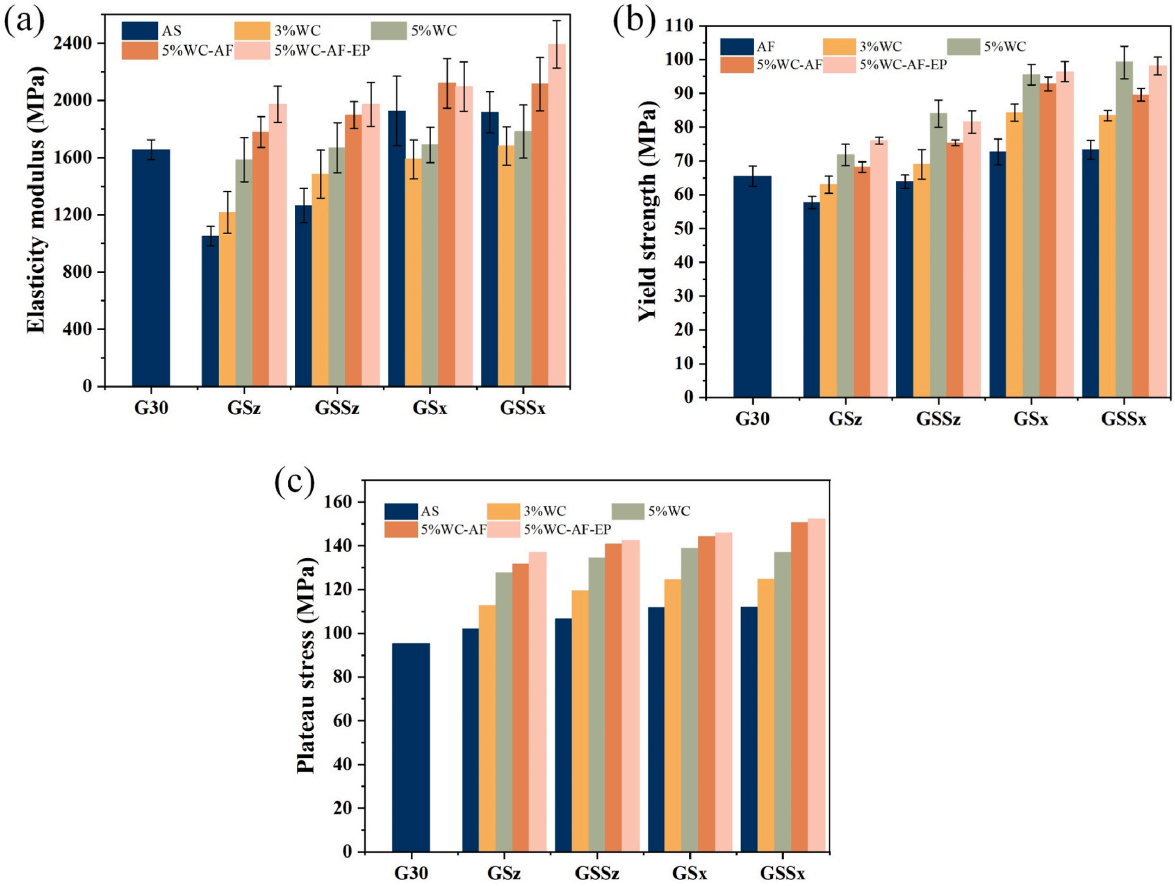

Fig. 8. Mechanical properties: (a) Modulus of elasticity; (b) Yield strength; (c) Plateau stress.

performance due to their consistent average ρ* across layers, leading to a more uniform distribution of stress and plastic strain compared to other samples. The elastic modulus represents the structural stiffness under deformation; therefore, during the elastic stage, the Gx structure can provide higher deformation resistance. The transition in relative density does not compromise the integrity of the Gx-type samples, and this different failure mechanism results in variations in mechanical performance.

In summary, the material and gradient design can optimize the mechanical properties of the lattice structure while keeping it lightweight.

3.3. Deformation patterns

The deformation behavior of the specimens responded to the effect of different structure types on the mechanical properties. The image of the Gyroid structure captured by the camera under strain (0, 0.15, 0.3, and 0.5) is shown in Fig. 9. Under stress, the lattice yields and collapses, and plastic hinge contacts are formed at the unit support sections or joints, which absorb a large amount of energy under approximately constant pressure.

Notably, the deformation behavior is primarily influenced by geometric gradient variations. Under compressive loading parallel to the gradient direction, Gz structures initially deform in regions with lower ρ*, exhibiting periodic collapse corresponding to variations in porosity. As deformation accumulates, after self-contact occurs in the low-ρ* regions, deformation progresses to involve regions with higher ρ*.

When the gradient direction is perpendicular to the compressive load, the change in gradient has no effect on the deformation, resembling uniform structures by exhibiting overall collapse. This is because Gx structures have consistent ρ* along the z-axis, which is equivalent to the layers being subjected to compressive stresses together. The GSz structure has a cycle of gradient change, i.e., there is a trough zone whose location corresponds to the ρ* minimum. During compression, the GSz structure first deforms in the upper part with higher porosity, with a rapid increase in strain, followed by a downward transfer, with a periodic trend of change with the value of the design function. The GSSz structure, on the other hand, has three trough zones, located on the two sides and in the middle, which leads to a gradual weakening of the hierarchical periodicity effect of the strain. Unlike the deformation behavior of conventional linear gradient structures, this nonlinear gradient structure exhibits periodic compressive deformation behavior. All samples did not fracture after compression, showing high toughness characteristics for energy absorption applications.

The Mises stress and LE strain distributions of the Gyroid structure at 20% strain were obtained from finite element simulations, as shown in Fig. 10. The results show that the stresses are mainly concentrated near the nodes. The uniform structural equivalent stress is lowest at the edges of the structure, while the stress concentration is larger at the center. Therefore, the deformation initially starts from the center region of the structure. For the Gx structure, a uniform stress distribution can be observed due to the uniform distribution of the ρ* in the y-z plane. This indicates that all the cells share the load and the gradient distribution perpendicular to the loading direction has no effect on the deformation characteristics of the structure. On the contrary, for the Gz structure, the stresses are concentrated in the regions with lower ρ* due to the gradation of the ρ* along the z-axis. Although cell layers with the same ρ* in different layers still bear equivalent stresses, only the part of cell layers with lower ρ* resist the load in the elastic phase, which further confirms the reason for the lower modulus of elasticity.

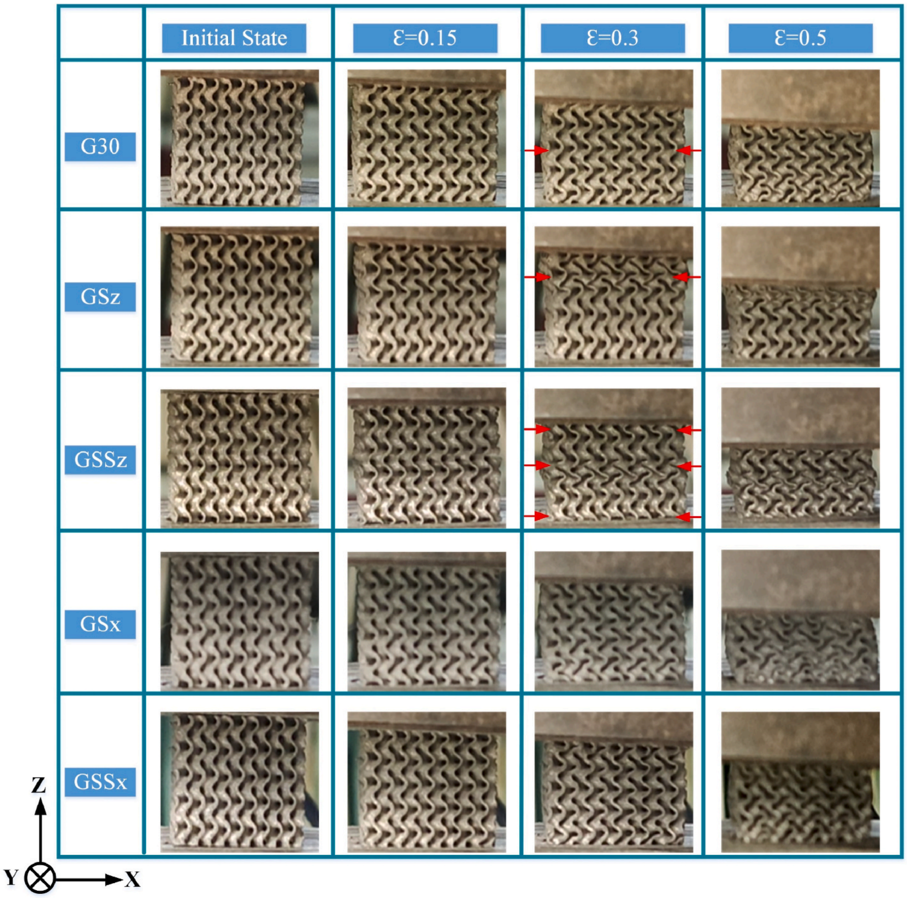

Fig. 9. Uniaxial compression test images of different Gyroid lattices at 0.2 strain level.

3.4. *Micro-organizational strengthening mechanisms*

Fig. S4 shows the phase composition of the samples detected by XRD analysis. According to the XRD results, the sample predominantly exhibits diffraction peaks corresponding to (111), (200), and (220), consistent with the austenite phase of 316L SS. The presence of WC phase was not detected due to the low WC addition. Therefore, the addition of WC did not alter the phase composition of 316L SS. To confirm the presence of WC, EDS analysis was conducted on the sample with 5 wt% WC addition, and its distribution is shown in Fig. 11.

Fig. 12(a–f) depict SEM images of 316L SS, 316L SS-5%WC, and 316L SS-5%WC-AF samples. The images reveal typical austenitic grain structures. Due to rapid melting and solidification during the LPBF process, this results in an uneven temperature distribution in the melt pool. The center of the melt pool typically has a higher temperature than the edges, leading to significant surface tension gradients and resulting in Marangoni convection [50]. This phenomenon causes cellular and dendritic grain growth within the melt pool [51,52]. In Fig. 12(c–d), WC is observed within the melt pool, closely integrated with the 316L SS matrix. Due to the extremely short duration of laser exposure and the high thermal conductivity of WC compared to 316L SS [53], significant temperature gradients form around the WC particles. These gradients facilitate the transfer and redistribution of heat flow within the melt pool, creating rapid solidification zones around the WC particles (Fig. 12 (d)), which promotes the formation of fine-grained microstructures. This refinement of grains is beneficial for optimizing the mechanical properties of the material. In Fig. 12(e–f), the application of AF results in clearer and straighter melt pool boundaries, revealing denser cellular and columnar substructures. This improvement is attributed to AF promoting convection and stirring within the melt pool, leading to a more uniform temperature distribution, which helps reduce microstructural inhomogeneities and subsequently enhances the mechanical properties [54,55].

Fig. 13 illustrates the grain orientation of 316L SS and 316L SS-5% WC specimens. As observed in Fig. 13(a–c), there are different grain orientations and grain sizes for the samples with and without WC. Due to the great temperature gradient generated during the LPBF process, grains typically grow in the direction of the maximum temperature gradient. Fig. 13 (a) shows the grain orientation of 316L SS, where the grains mainly show columnar crystals with major grain orientations of <001> and <111>. The inverse pole figure(IPF) (Fig. 13 (m)) confirms a strong <001> orientation in the build direction (BD), with a maximum texture index of 6.14. When the grain orientation tends toward <001>, the samples exhibit poorer mechanical properties [56]. With the addition of 5% WC (Fig. 13 (b)), significant grain refinement is observed, promoting a transition from columnar to equiaxed grains. The grain orientation shifts from predominantly <001> to a coexistence of <001>, <101>, and <111>. This change reduced the texture index to 2.58 (Fig. 13 (n)), weakening the texture and reducing stress concentration, which leads to more isotropic mechanical properties. Although the addition of 5% WC and the application of AF lead to a tendency toward <001> orientation, the maximum texture index is only 2.04. For FCC phase 316L SS, the mechanical properties of grains oriented in <101> and <111> directions are superior to those in the <001> direction. This is a key reason why the mechanical properties of the material are optimized with the addition of WC [57,58].

From Fig. 13(d–f), it can be seen that, compared to the 316L SS samples (with an average grain size of 11.46 μm), the grain size decreases to 6.82 μm after the addition of 5% WC, and further decreases to 4.11 μm with the application of AF. This reduction in grain size is

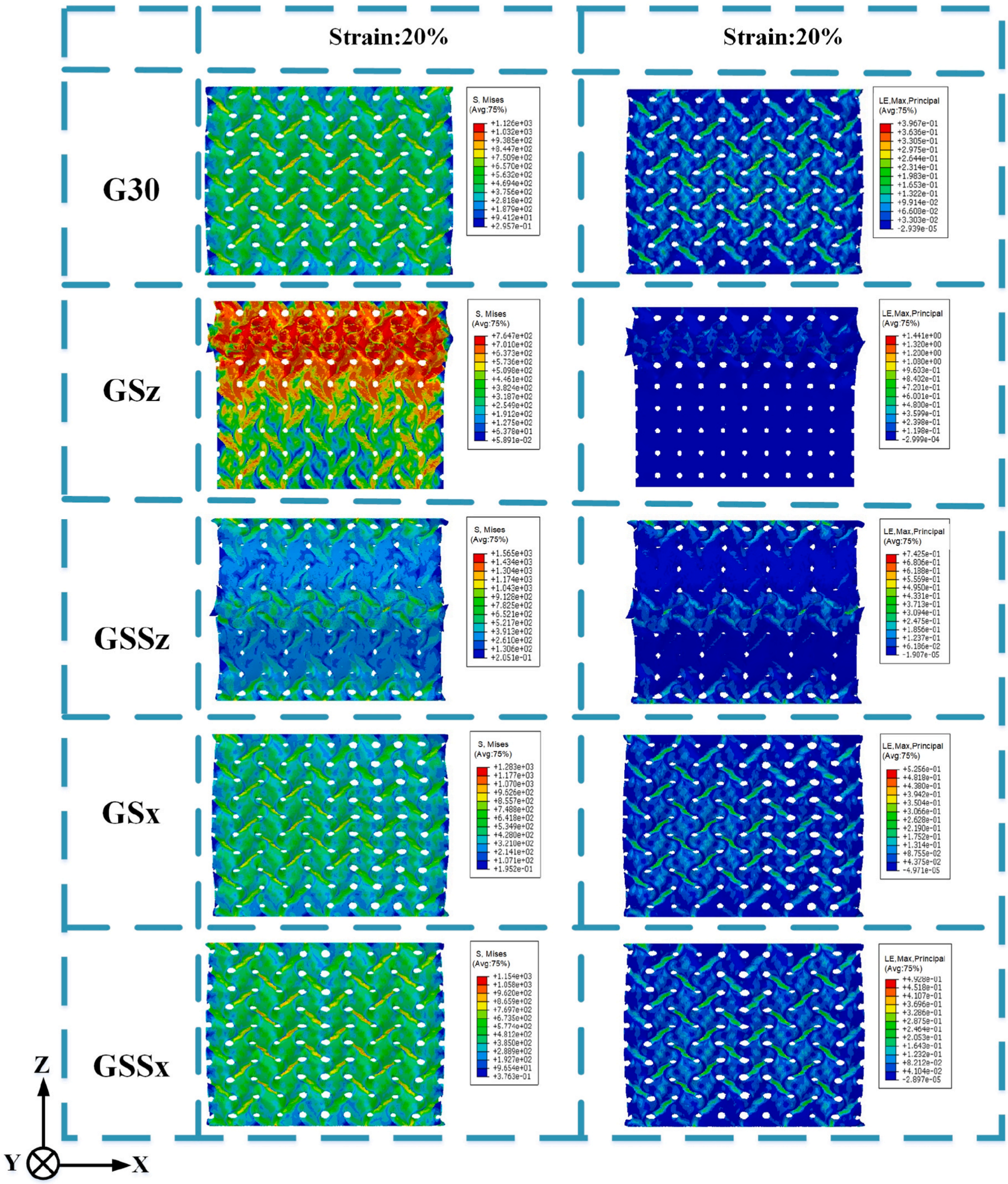

Fig. 10. Von Mises stress and LE strain distribution of Gyroid structure at 20% strain.

attributed to the heterogeneous nucleation points formed by WC, which promote grain refinement, along with the acoustic streaming and cavitation effects generated by AF, which reduce the temperature gradient and facilitate nucleation while inhibiting grain growth. This further demonstrates that WC can increase the number of grain boundaries, effectively impeding the propagation of dislocations and cracks, thus contributing positively to the enhancement of strength. Additionally, the application of AF promotes melt pool flow, further validating its role in reducing the temperature gradient that influences grain refinement.

Grain boundary orientation difference is another crucial indicator of the microstructural characterization of the material, typically classified into low-angle grain boundaries (LAGBs, angle <15°) and high-angle grain boundaries (HAGBs, angle >15°). Fig. 13(g–l) show the histogram of the number and orientation angle distribution of HAGBs and LAGBs. After the addition of 5% WC and the application of AF, the proportion of HAGBs significantly increased to 62.8%, compared to only 19.0% in the 316L SS samples. This difference is attributed to the grain refinement caused by the addition of WC, which increases the density of HAGBs. On the other hand, the presence of large thermal stresses, shrinkage stresses, and phase transformation stresses during the LPBF process induces localized plastic deformation. The application of AF facilitates the gradual evolution of previously formed LAGBs into HAGBs [59,60]. HAGBs can impede dislocation motion, thereby enhancing the strength of the material.

The distribution of the recrystallized grains (blue) and substructure grains (yellow) is shown in Fig. S5. The addition of WC particles and the

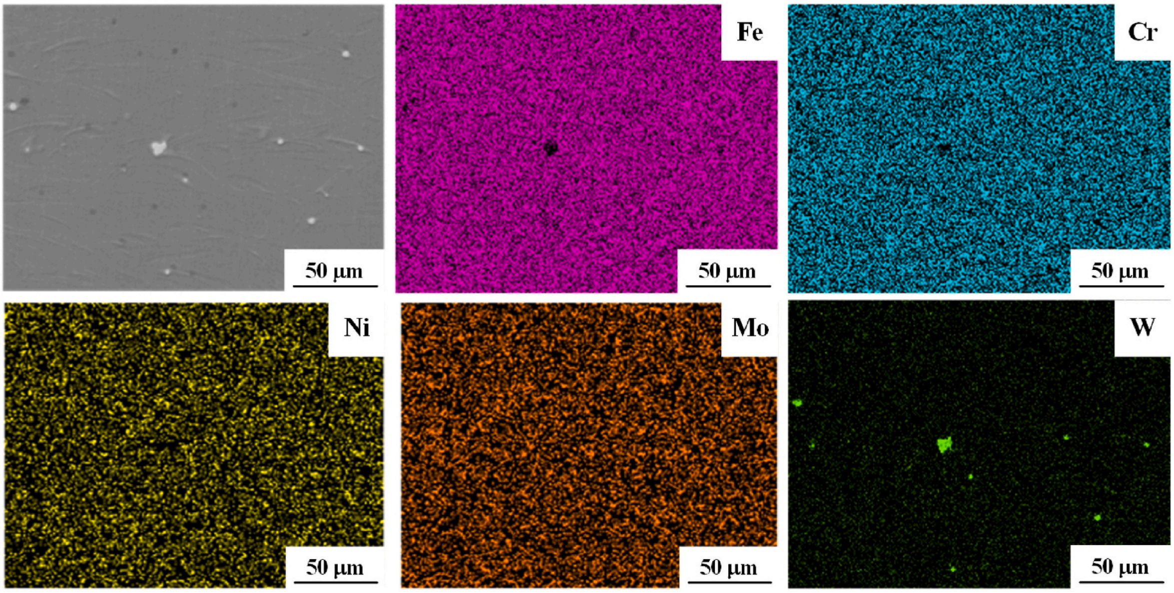

Fig. 11. SEM micrographs and corresponding EDS of 316L SS-5%WC samples.

application of AF facilitated recrystallization during the LPBF process. After adding 5 wt% WC particles and applying AF, the proportion of recrystallization increased to 7.3%. This further indicates that the WC particles in the melt pool act as heterogeneous nucleation sites [61]. In this process, the transition from LAGB to HAGB is facilitated by the increase in subgrain rotation and grain boundary misorientation angle [62]. The HAGBs and WC particles provide effective barriers for the growth of recrystallized grains, allowing dislocations to remain at the HAGBs.

Fig. 14 shows the kernel average misorientation (KAM). KAM is closely related to LAGBs and HAGBs, regions with a high density of LAGBs indicate significant dislocation accumulation, resulting in higher KAM values. Conversely, regions with a high density of HAGBs exhibit lower KAM values. After the addition of WC, the average of KAM decreased from 0.56° to 0.52°, while the average of KAM remained unchanged with the application of AF. This indicates that both WC and the application of AF can improve dislocation accumulation, thereby reducing the generation of stress concentrations to some extent.

Fig. 15 shows the mechanism of acoustic field influence on the molten pool during the LPBF process. The blue arrow indicates the direction of heat conduction, which is opposite to the direction of grain growth. When no acoustic field is applied, the grains grow as columnar crystals perpendicular to the solid-liquid interface in the opposite direction of heat conduction. After the introduction of the acoustic field, the acoustic flow has a significant effect on grain refinement. Argon as a protective gas, and the melt pool solution acoustic impedance is different, under the action of the acoustic field, the interface due to acoustic energy reflection, refraction to produce a pressure difference, drive the liquid metal in the melt pool to form an acoustic flow. This acoustic flow will change the natural convection pattern originally caused by surface tension gradient and laser. The acoustic flow induced by the acoustic field creates additional annular or vortex flow in the liquid metal in the melt pool, accelerating the migration of solute atoms and making the composition of the melt pool more homogeneous. At the same time, it quickly disperses the localized heat accumulation, suppresses the temperature gradient, and promotes uniform heating. Entering the solidification stage, the acoustic flow breaks the growing larger grains through fluid shear, and triggers local energy and composition fluctuations, generating more nucleation sites, and ultimately effectively refining the grains.

In short, the mechanical properties of the material are influenced by KAM, grain size, and texture index. When the grain orientation in the IPF is uniform and the grain size and KAM are low, the samples will exhibit optimal mechanical properties. In these aspects, the WC composite structures with the application of AF outperform the original structures.

Fig. 16 presents the morphological characteristics and thickness of the polymer coating analyzed by SEM. In Fig. 16 (a), red arrows and dashed lines indicate the coating surface. The cross-section of the coated structure reveals two distinct regions with a clearly identifiable interface. The impregnating agent covers the structure surface, forming an epoxy layer with a thickness of 30~60 μm. The coating adhered well to the substrate, effectively filling micropores on the structure surface. The polymer coating improves the deformation resistance of the structure by effectively physically interlocking with the rigid TPMS structure to form a coherent interface. In contrast, the SEM image of the uncoated TPMS surface in Fig. 16 (b) shows a higher surface roughness. These results indicate that enhancing the deformation resistance of TPMS structures by filling their surface micropores with polymers to form a homogeneous physical interlock is an effective method of extrinsic reinforcement.

3.5. Energy absorption

The cumulative energy absorption per unit volume (W_v), calculated by numerical integration method:

$$W_v = \int_0^{\varepsilon_d} \sigma(\varepsilon) d\varepsilon \tag{4}$$

where σ(ε) is the stress associated with ε and ε_d is the densification strain.

During the deformation of lattice structures, energy absorption is usually quantified and ε_d is considered as the practical limit of energy absorption applied to lattice structures [63]. There are two ways to determine ε_d: (i) the maximum value of the efficiency curve of the hardened structure; and (ii) the strain corresponding to the peak of the energy absorption efficiency defined for fully plastic structures [64]. Since the fabricated Gyroid structures do not undergo brittle fracture and exhibit plastic deformation throughout the deformation process, the second method is used to calculate ε_d, defined as follows:

$$\eta(\varepsilon) = \frac{1}{\sigma(\varepsilon)} \int_0^{\varepsilon} \sigma(\varepsilon) d\varepsilon \tag{5}$$

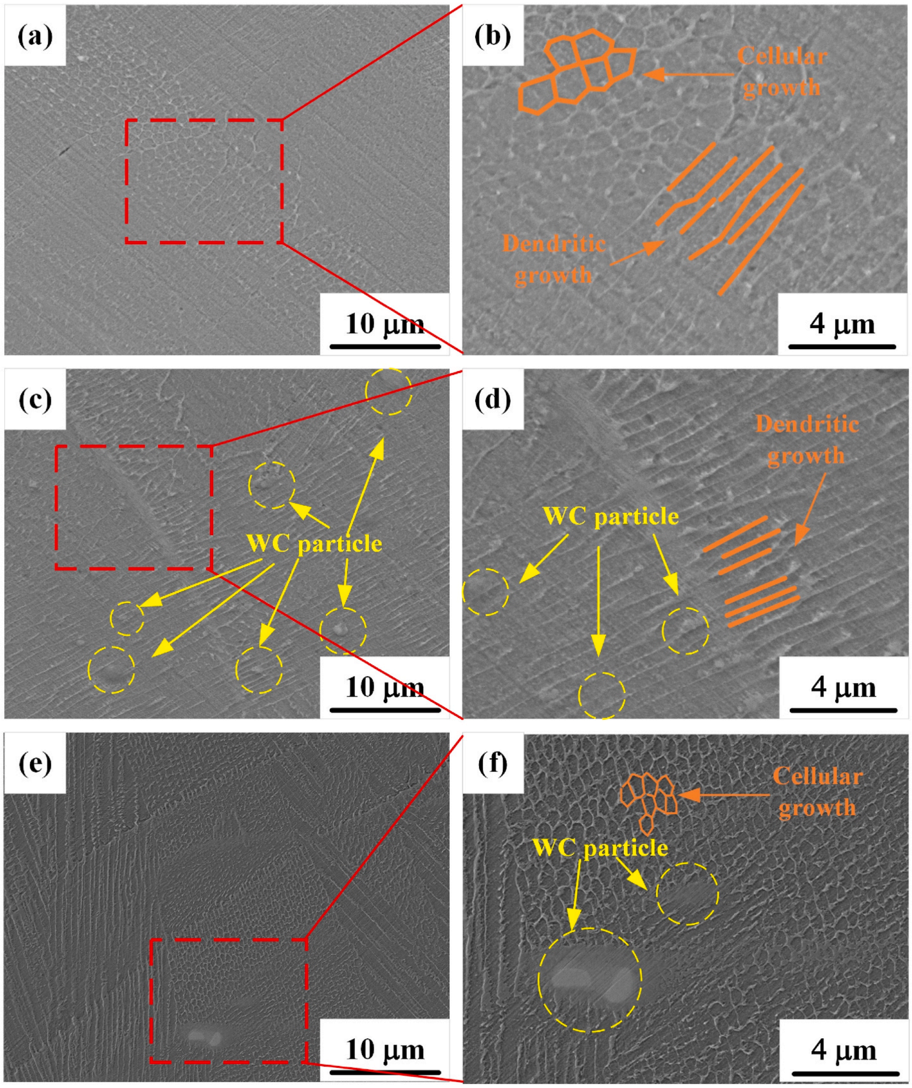

Fig. 12. SEM images of (a) 316L SS; (b) localized high magnification images in (a); (c) 316L SS-5%WC; (d) localized high magnification images in (c); (e) 316L SS-5% WC-AF; (f) localized high magnification images in (e).

$$\left.\frac{d\eta(\varepsilon)}{d\varepsilon}\right|_{\varepsilon=\varepsilon_d}=0 \tag{6}$$

SEA indicates the amount of energy absorbed per unit mass of a structure and is an important measure of energy absorption.

$$E=\int_0^{S_{ef}} F(s)ds \tag{7}$$

$$\mathrm{SEA}=\frac{E}{M} \tag{8}$$

where S_{ef} is the displacement corresponding to the densification strain, F (S) and S are the force and displacement acting on the structure, respectively, E is the energy absorption, and M represents the mass of the structure. Taking the G30 structure as an example, Fig. 17 illustrates the relationship between force and energy absorption.

Fig. 18 and Fig. S3 show the $W_v - \varepsilon$ curves for gradient and uniform lattice structures. These curves are fitted with a function whose fitting exponent represents the growth rate of W_v under compressive loading [65]. It can be observed that the fitting exponent for the Gz sample is higher than that of the Gx and uniform samples, indicating that the energy absorption characteristic of Gz sample is better than that of Gx sample. The main reason for this is that during compression, the layer-by-layer deformation of the Gz structure and the gradual increase in its load-bearing capacity enable it to absorb more energy. This gradient structural design effectively regulates the transfer and distribution of stresses by providing different stiffnesses and strengths in different areas, and this stress distribution helps to improve the overall energy absorption capacity of the structure. For example, Choy et al. [66] studied the energy absorption capacities of honeycomb and cubic lattices with different diameters and densities, finding that the exponent values for gradient structures were higher than those for their respective uniform structures. The results of the study show that the direction of the gradient has a significant effect on the index value. Different gradient distributions lead to different deformation patterns between the structures, which affects the energy absorption. Therefore, varying the gradient direction can modulate the lattice structure energy absorption.

Although the designed Gyroid lattice structures have the same ρ*, their densification strain is significantly influenced by the gradient distribution. As shown in Fig. 9, the Gz samples has a large densification strain. In contrast, the Gx structure, due to its ρ* gradient being perpendicular to the load direction, has a lower overall densification strain. After adding WC, the energy absorption of all samples improved to varying degrees. Among them, the GSSz-5%WC-AF sample had the highest W_v at 109.17 MJ/m^3, which is 51.16% higher than the GSSz

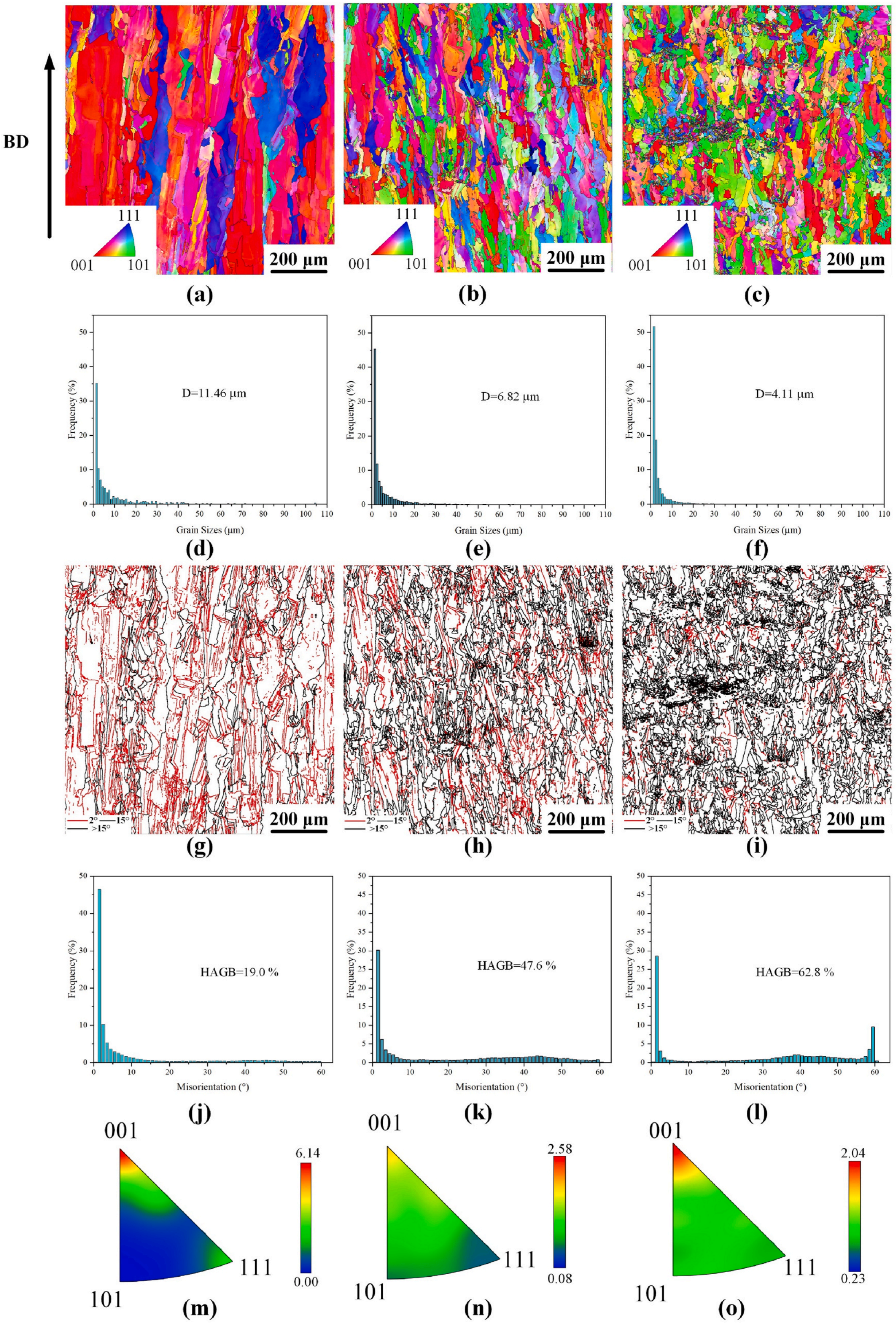

Fig. 13. EBSD analysis of Gyroid samples under conditions without the WC and with 5 wt% WC. (a) Grain orientation of the 316L SS, (b) 316L SS-5%WC and (c) 316L SS-5%WC-AF. (d) Grain size distribution of the 316L SS, (e) 316L SS-5%WC and (f) 316L SS-5%WC-AF. (g) Grain boundary of the 316L SS, (h) 316L SS-5%WC and (i) 316L SS-5%WC-AF. (j) Grain boundary distribution histograms of the 316L SS, (k) 316L SS-5%WC and (l) 316L SS-5%WC-AF. (m) IPF of the 316L SS, (n) 316L SS-5%WC and (o) 316L SS-5%WC-AF.

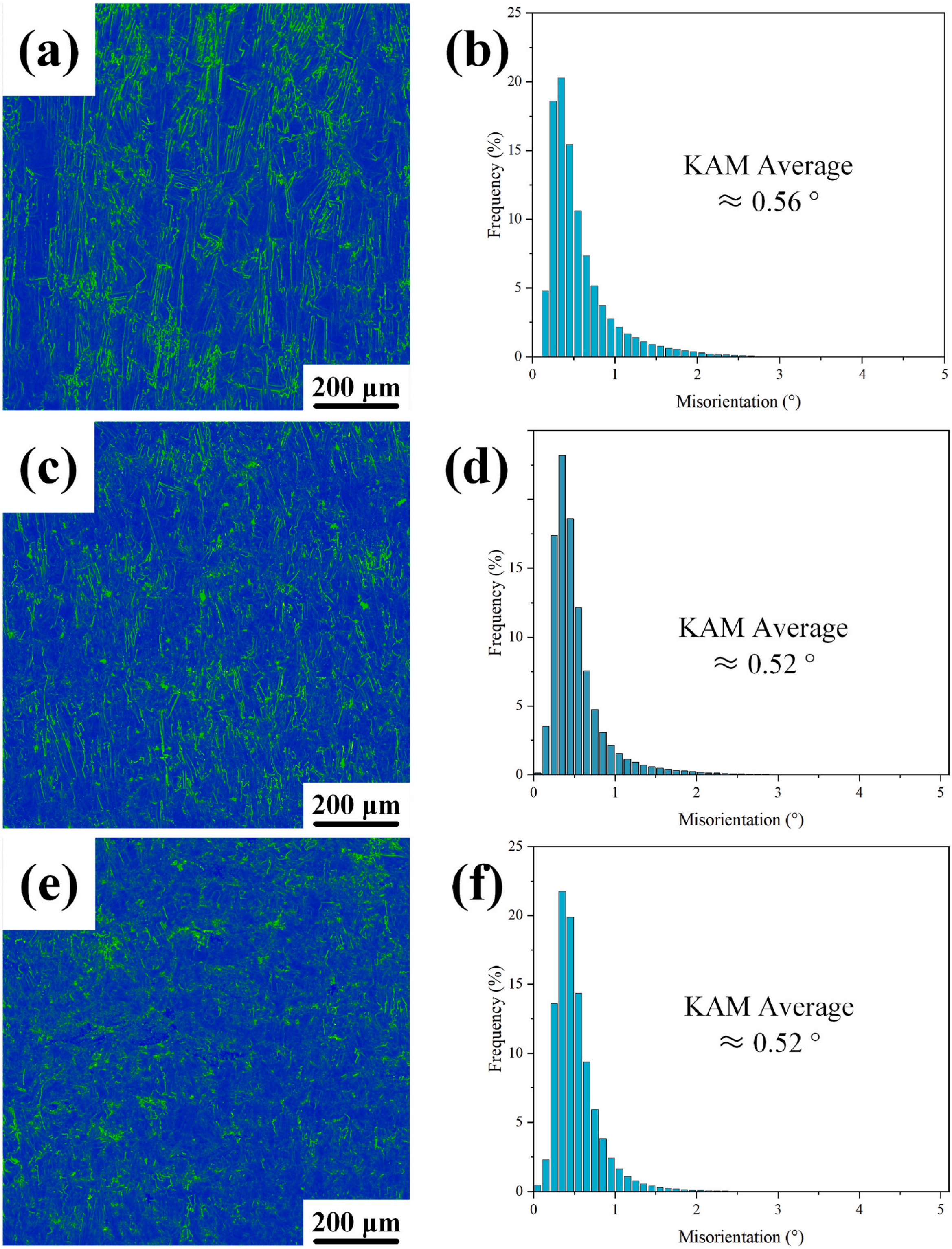

Fig. 14. KAM distribution histograms of 316L SS (a, b), 5 wt% WC/316L SS (c, d), and 316L SS-5%WC-AF (e, f).

sample, 87.55% higher than the G30 sample, and 26.44% higher than the G40 sample. Despite the samples coated with the impregnating agent having the highest plateau stress, Table 2 shows that the coating reduced the densification strain of the samples, resulting in slightly lower energy absorption compared to the samples prepared with composite materials. This is due to the fact that the coating leachate affects the structural porosity to some extent. Usually the energy absorption of a structure is obtained from the strain before densification, and the coating causes the structure to densify earlier, but the reduction in energy absorption is limited. The purpose of coating with an immersion agent is to allow the structure to provide greater resistance to deformation in the small strain range and protection from large strains on large deformations. This approach provides a good trade-off in terms of energy absorption.

To evaluate the energy absorption performance of the designed TPMS, the results of this study were compared with experimental results from the literature. As shown in Fig. 19, the GSSz-5%WC-AF sample in

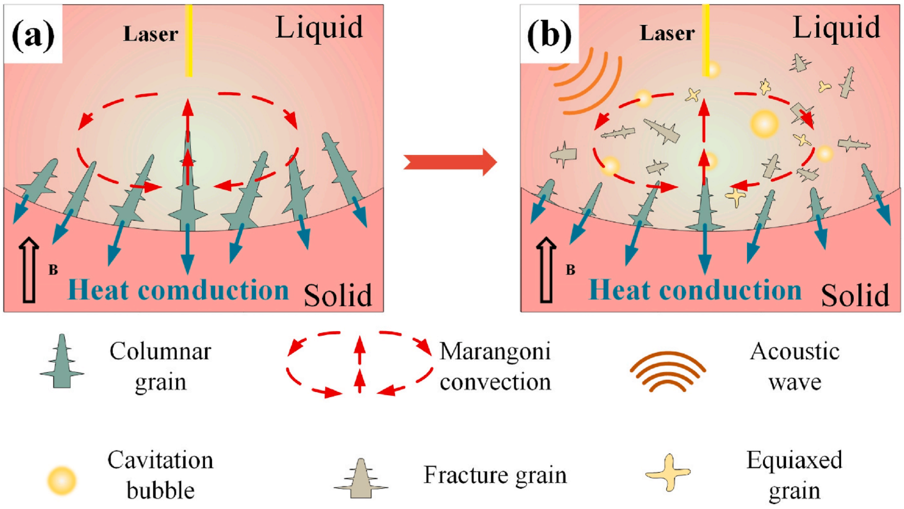

Fig. 15. Schematic diagram of the evolution of acoustic fields auxiliary organization.

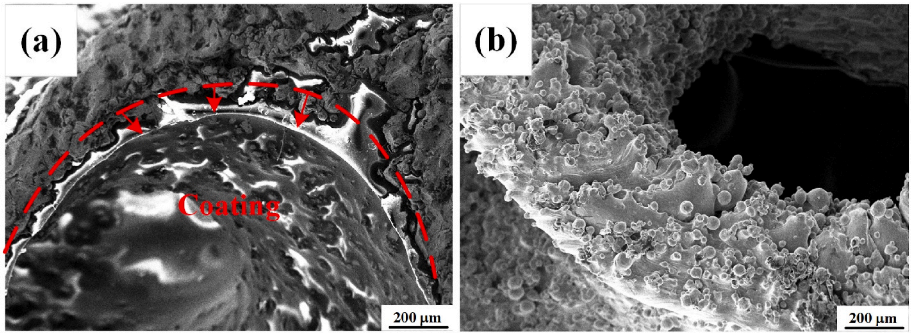

Fig. 16. SEM image of the lattice surface of Gyroid: (a) Morphology of the coated surface and (b) Uncoated surface morphology.

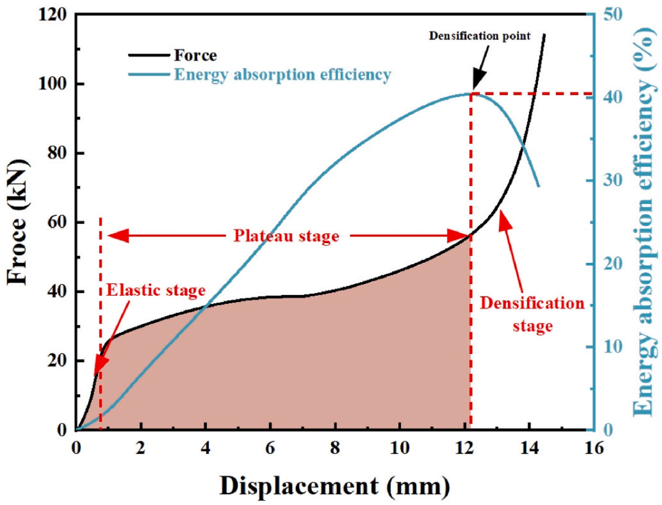

Fig. 17. Definition of mechanical indicators based on force-displacement curves.

this study exhibited the highest SEA, reaching 43.54 J/g. This represents a 76.78% increase compared to the uniform G30 structure of 24.63 J/g and a 55.33% increase compared to the G40 structure of 28.03 J/g. Clearly, the GSSz lattice with a 30% ρ* designed in this study demonstrates significant potential in terms of energy absorption.

In summary, this study proposes an internal and external reinforcement method for lattice structures by introducing AF to fabricate composite lattice structures and applying a permeating agent, significantly enhancing their mechanical properties. The addition of AF and WC results in grain refinement and texture weakening. WC particle reinforcement significantly improves the toughness of the structure by increasing the hardness and resistance to crack extension of the material. WC particles are able to increase the compressive strength of the material by refining the grains and enhancing the interfacial bonding, which increases the ability to carry external loads. The enhancement of mechanical properties is mainly duo to the optimization of the microstructure and the resistance to deformation provided by the external physical interlocking structure. Overall, the IPCs lattice structure designed in this study enhances mechanical properties while ensuring lightweight construction.

4. Conclusions

In this work, Gyroid lattices with excellent mechanical properties were prepared using the LPBF process in combination with AF. The print quality of the fabricated samples was evaluated by SEM, and the mechanical response and microstructure strengthening mechanisms of the pristine and composite structures were explored via compression tests, finite element simulations, and EBSD. The major conclusions are presented as follows.

(1) The SEM revealed that the Gyroid structures fabricated using the LPBF process exhibited good print quality, with no obvious defects. However, due to structural design and process

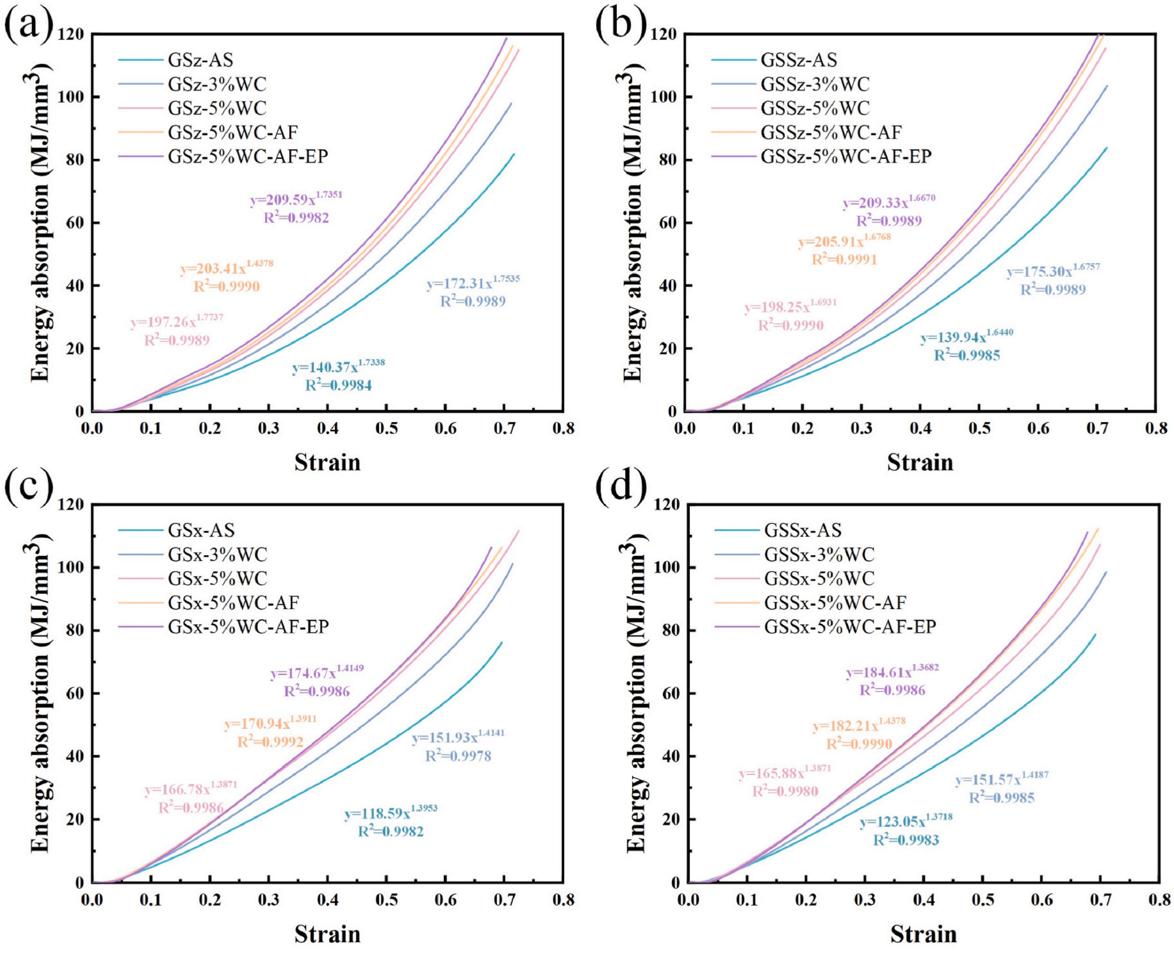

Fig. 18. Energy absorption curves of: (a) GSz; (b) GSSz; (c) GSx and (d) GSSx.

Table 2
Gyroid structure energy absorption.

	GSz		GSSz		GSx		GSSx	
	ε_d	W_v (MJ/m^3)	ε_d	W_v (MJ/m^3)	ε_d	W_v (MJ/m^3)	ε_d	W_v (MJ/m^3)
AS	0.6594	68.35	0.6656	72.22	0.5831	54.84	0.5882	58.54
3%WC	0.6683	90.24	0.6524	90.31	0.5997	74.83	0.6169	78.91
5%WC	0.6713	97.75	0.6793	104.09	0.6276	86.54	0.6108	85.47
5%WC-AF	0.6757	103.40	0.6799	109.17	0.6234	88.29	0.6096	88.49
5%WC-AF-EP	0.6420	97.56	0.6326	97.22	0.5842	80.44	0.5985	85.13

characteristics, there is powder adhesion on the surface, which leads to some deviation of the print from the designed sample.

(2) The improved Gyroid lattice outperformed the original Gyroid lattice in both strength and SEA, exhibiting excellent energy absorption performance. The SEA of the GSSz-5% WC-AF sample reached up to 43.54 J/g, which is approximately 76.78% higher than that of the G30 lattice.

(3) The WC and the application of AF resulted in significant grain refinement and weakened texture intensity. The introduction of WC particles promotes the formation of grain boundaries, thereby optimizing the microstructure of the structure and enhancing its mechanical properties.

(4) The composite structure exhibited a densification strain of up to ~0.67. The combination of high densification strain and high plateau stress endowed the lattice with superior energy absorption capacity. Although the coating of the impregnating agent contributed to the strength, it also led to earlier densification, resulting in a slightly lower SEA compared to the composite structure.

CRediT authorship contribution statement

Shuai Guo: Conceptualization, Data curation, Writing – original draft. **Xianliang Sheng:** Conceptualization, Data curation, Investigation, Writing – original draft. **Anfu Guo:** Investigation, Methodology, Writing – review & editing. **Wenlu Yang:** Methodology. **Xiaolin Zhao:** Resources. **Shang Sui:** Methodology, Software. **Jiaqiang Li:** Data curation, Investigation. **Yufan Zhao:** Data curation, Formal analysis. **Meng Wang:** Conceptualization, Investigation. **Xin Lin:** Supervision, Writing – review & editing.

Data availability

Data will be made available on request.

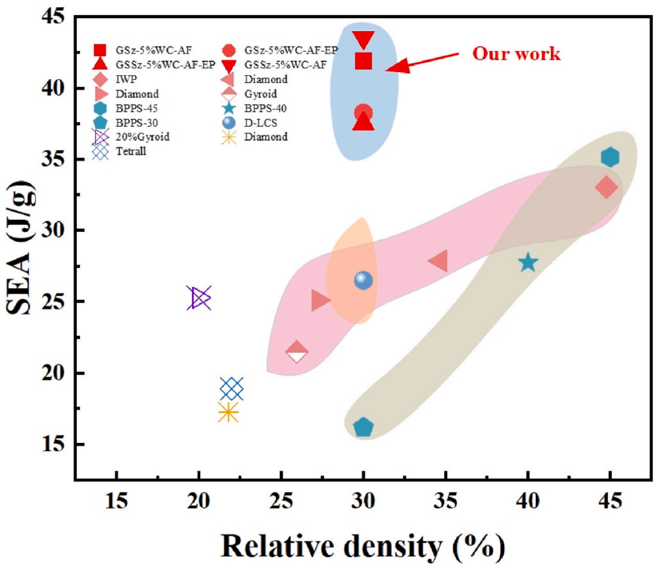

Fig. 19. SEA of our work and literature [17,21,67–70].

Declaration of competing interest

The authors declare that they have no known competing financial interests or personal relationships that could have appeared to influence the work reported in this paper.

Acknowledgement

This work was supported by the National Key Research and Development Program of China (No. 2022YFB4602301), the National Natural Science Foundation of China (No. 52405371, No. 52301207, No. 52275381), and the Key Research and Development Program of Shaanxi Province (No. 2021LLRH-08). We also thank Mr. Conghua qi of Shiyanjia Lab (www.shiyanjia.com) for the XRD test.

Appendix A. Supplementary data

Supplementary data to this article can be found online at https://doi.org/10.1016/j.jmrt.2025.01.191.

References

[1] Chen J, Hu L, Wu J, Yan Z, Chen Y, He C, Ai S. Bilayer lattice structure integrated with phase change material for innovative thermal protection system design. Aero Sci Technol 2023;141:108576. https://doi.org/10.1016/j.ast.2023.108576.

[2] Sheng X, Guo A, Guo S, Sui S, Yang W, Tang R, Li X, Qu P, Wang M, Lin X. Laser powder bed fusion for the fabrication of triply periodic minimal surface lattice structures: synergistic macroscopic and microscopic optimization. J Manuf Process 2024;119:179–92. https://doi.org/10.1016/j.jmapro.2024.03.081.

[3] Wang S, Li S, Zhai Z, Guo A, Qu P, Yang G, Shao S. Bending performance and failure modes of sinusoidal corrugated sandwich panels fabricated using stereolithography technology: effects of geometric parameters. Eng Fail Anal 2024;158:107987. https://doi.org/10.1016/j.engfailanal.2024.107987.

[4] Hou W, He P, Yang Y, Sang L. Crashworthiness optimization of crash box with 3D-printed lattice structures. Int J Mech Sci 2023;247:108198. https://doi.org/10.1016/j.ijmecsci.2023.108198.

[5] Surjadi JU, Gao L, Du H, Li X, Xiong X, Fang NX, Lu Y. Mechanical metamaterials and their engineering applications. Adv Eng Mater 2019;21:1800864. https://doi.org/10.1002/adem.201800864.

[6] Kong D, Guo A, Wu H, Li X, Wu J, Hu Y, Qu P, Wang S, Guo S. Four-dimensional printing of polymer-derived ceramics with high-resolution, reconfigurability, and shape memory effects. Addit Manuf 2024;83:104050. https://doi.org/10.1016/j.addma.2024.104050.

[7] Qi C, Jiang F, Yang S. Advanced honeycomb designs for improving mechanical properties: a review. Compos B Eng 2021;227:109393. https://doi.org/10.1016/j.compositesb.2021.109393.

[8] Hunt CJ, Morabito F, Grace C, Zhao Y, Woods BKS. A review of composite lattice structures. Compos Struct 2022;284:115120. https://doi.org/10.1016/j.compstruct.2021.115120.

[9] Guo S, Zhao Y, Sui S, Zhu P, Wang M, Hao X, Song Y, Guo A, Ni J, Qin Y, Lin X. Effect of static magnetic field on the chemical short-range order of CoCrFeMnNi high-entropy alloy prepared by laser powder bed fusion. Intermetallics 2024;175:108498. https://doi.org/10.1016/j.intermet.2024.108498.

[10] Zhai Z, Wang S, Yang G, Guo A, Qu P, Song Y, Shao S, Zang J. Novel sandwich structures with double-row and crossed pyramidal lattice cores: design, fabrication and bending behavior. Eng Fail Anal 2025;170:109267. https://doi.org/10.1016/j.engfailanal.2025.109267.

[11] Guo A, Tang R, Guo S, Hu Y, Sheng X, Zhang Y, Zhang M, Qu P, Wang S. Acoustic field-assisted powder bed fusion of tungsten carbide-reinforced 316L stainless steel composites. J Mater Res Technol 2023;26:5488–502. https://doi.org/10.1016/j.jmrt.2023.08.271.

[12] Feng J, Fu J, Yao X, He Y. Triply periodic minimal surface (TPMS) porous structures: from multi-scale design, precise additive manufacturing to multidisciplinary applications. Int J Extrem Manuf 2022;4:022001. https://doi.org/10.1088/2631-7990/ac5be6.

[13] Benedetti M, du Plessis A, Ritchie RO, Dallago M, Razavi N, Berto F. Architected cellular materials: a review on their mechanical properties towards fatigue-tolerant design and fabrication. Mater Sci Eng R Rep 2021;144:100606. https://doi.org/10.1016/j.mser.2021.100606.

[14] Yang L, Yan C, Cao W, Liu Z, Song B, Wen S, Zhang C, Shi Y, Yang S. Compression–compression fatigue behaviour of gyroid-type triply periodic minimal surface porous structures fabricated by selective laser melting. Acta Mater 2019;181:49–66. https://doi.org/10.1016/j.actamat.2019.09.042.

[15] Jin J, Wu S, Yang L, Zhang C, Li Y, Cai C, Yan C, Shi Y. Ni–Ti multicell interlacing Gyroid lattice structures with ultra-high hyperelastic response fabricated by laser powder bed fusion. Int J Mach Tool Manufact 2024;195:104099. https://doi.org/10.1016/j.ijmachtools.2023.104099.

[16] Zhang L, Feih S, Daynes S, Chang S, Wang MY, Wei J, Lu WF. Energy absorption characteristics of metallic triply periodic minimal surface sheet structures under compressive loading. Addit Manuf 2018:23. https://doi.org/10.1088/1742-6596/2535/1/012025.

[17] Li L, Gu D, Liu H, Zhang H, Shan J, Zhang Y. Lightweight load-bearing heat dissipation multifunctional pomelo peel-inspired structures fabricated by laser powder bed fusion. International Journal of Bioprinting 2023;9:1011. https://doi.org/10.36922/ijb.1011.

[18] Siddique SH, Hazell PJ, Wang H, Escobedo JP, Ameri AAH. Lessons from nature: 3D printed bio-inspired porous structures for impact energy absorption – a review. Addit Manuf 2022;58:103051. https://doi.org/10.1016/j.addma.2022.103051.

[19] Cheng L, Bai J, To AC. Functionally graded lattice structure topology optimization for the design of additive manufactured components with stress constraints. Comput Methods Appl Mech Eng 2019;344:334–59. https://doi.org/10.1016/j.cma.2018.10.010.

[20] Wu S, Yang L, Yan C, Shi Y. Fatigue properties of SiC graded ceramic lattice structures with a triply periodic minimal surface manufactured by laser powder bed fusion. J Eur Ceram Soc 2024;44:116695. https://doi.org/10.1016/j.jeurceramsoc.2024.116695.

[21] Yang L, Mertens R, Ferrucci M, Yan C, Shi Y, Yang S. Continuous graded Gyroid cellular structures fabricated by selective laser melting: design, manufacturing and mechanical properties. Mater Des 2019;162:394–404. https://doi.org/10.1016/j.matdes.2018.12.007.

[22] Wang Y, Liu F, Zhang X, Zhang K, Wang X, Gan D, Yang B. Cell-size graded sandwich enhances additive manufacturing fidelity and energy absorption. Int J Mech Sci 2021;211:106798. https://doi.org/10.1016/j.ijmecsci.2021.106798.

[23] Wang X, Gao T, Shi C, Zhou Y, Li Z, Wang Z. Effect of geometric configuration on compression behavior of 3D-printed polymeric triply periodic minimal surface sheets. Mech Adv Mater Struct 2023;30:2304–14. https://doi.org/10.1080/15376494.2022.2053906.

[24] Qiu N, Wan Y, Shen Y, Fang J. Experimental and numerical studies on mechanical properties of TPMS structures. Int J Mech Sci 2024;261:108657. https://doi.org/10.1016/j.ijmecsci.2023.108657.

[25] Morrish SJN, Pedersen M, Wong KFW, Todd I, Goodall R. Size effects in compression in Electron Beam Melted Ti6Al4V diamond structure lattices. Mater Lett 2017;190:138–42. https://doi.org/10.1016/j.matlet.2016.12.130.

[26] Zhai Z, Wang S, Li S, Guo A, Qu P, Song Y, Yang G, Shao S, Tang R. An experimental and numerical investigation into compressive failure of pyramidal lattice sandwich structures fabricated using stereolithography technology. Fatig Fract Eng Mater Struct 2024;47:2823–40. https://doi.org/10.1111/ffe.14322.

[27] Luo Y, Hu SP, Liu YZ, Wang YX, Song XG, Cao J. Fabrication and mechanical properties of three-dimensional enhanced TiAl/GH3536 hetero-honeycomb sandwich structure. J Mater Res Technol 2023;26:7490–501. https://doi.org/10.1016/j.jmrt.2023.09.064.

[28] Zhang J, Song B, Yang L, Liu R, Zhang L, Shi Y. Microstructure evolution and mechanical properties of TiB/Ti6Al4V gradient-material lattice structure fabricated by laser powder bed fusion. Compos B Eng 2020;202:108417. https://doi.org/10.1016/j.compositesb.2020.108417.

[29] Guo A, Kong D, Zhou X, Kong H, Qu P, Wang S, Wang H, Hu Y. Method for preparing damage-resistant 3D-printed ceramics via interior-to-exterior strengthening and toughening. Addit Manuf 2022;60:103272. https://doi.org/10.1016/j.addma.2022.103272.

[30] Hohe J, Beckmann C, Böhme W, Weise J, Reinfried M, Luthardt F, Rapp F, Diemert J. An experimental and numerical survey into the potential of hybrid

foams. Mech Mater 2019;136:103063. https://doi.org/10.1016/j.mechmat.2019.103063.
[31] Guo X, Ding J, Li X, Qu S, Hsi Fuh JY, Lu WF, Song X, Zhai W. Interpenetrating phase composites with 3D printed triply periodic minimal surface (TPMS) lattice structures. Compos B Eng 2023;248:110351. https://doi.org/10.1016/j.compositesb.2022.110351.
[32] Jhaver R, Tippur H. Processing, compression response and finite element modeling of syntactic foam based interpenetrating phase composite (IPC). Materials Science and Engineering: A 2009;499:507–17. https://doi.org/10.1016/j.msea.2008.09.042.
[33] Duarte I, Vesenjak M, Krstulović-Opara L, Ren Z. Crush performance of multifunctional hybrid foams based on an aluminium alloy open-cell foam skeleton. Polym Test 2018;67:246–56. https://doi.org/10.1016/j.polymertesting.2018.03.009.
[34] Li X, Tan YH, Wang P, Su X, Willy HJ, Herng TS, Ding J. Metallic microlattice and epoxy interpenetrating phase composites: experimental and simulation studies on superior mechanical properties and their mechanisms. Compos Appl Sci Manuf 2020;135:105934. https://doi.org/10.1016/j.compositesa.2020.105934.
[35] Bi J, Chi J, Song H, Shao H, Wang K, Yang Z, Jia X, Dong G. Enhancing tensile properties of MIG welded AA6061 joints: effect of pulse mode and post-weld heat treatment. Mater Today Commun 2024;39:109156. https://doi.org/10.1016/j.mtcomm.2024.109156.
[36] Chi J, Shao H, Song H, Wang X, Wu K, Zheng Q, Dmitrievich Starostenkov M, Dong G, Bi J. Effect of double-pulse frequency and post-weld heat treatment on microstructure and mechanical properties of metal-inert gas welded Al–Mg–Si alloy joints. Materials Science and Engineering: A 2024;913:147029. https://doi.org/10.1016/j.msea.2024.147029.
[37] Tan C, Li R, Su J, Du D, Du Y, Attard B, Chew Y, Zhang H, Lavernia EJ, Fautrelle Y, Teng J, Dong A. Review on field assisted metal additive manufacturing. Int J Mach Tool Manufact 2023;189:104032. https://doi.org/10.1016/j.ijmachtools.2023.104032.
[38] Hu Y. Recent progress in field-assisted additive manufacturing: materials, methodologies, and applications. Mater Horiz 2021;8:885–911. https://doi.org/10.1039/D0MH01322F.
[39] Ning F, Cong W. Microstructures and mechanical properties of Fe-Cr stainless steel parts fabricated by ultrasonic vibration-assisted laser engineered net shaping process. Mater Lett 2016;179:61–4. https://doi.org/10.1016/j.matlet.2016.05.055.
[40] Wang H, Hu Y, Ning F, Cong W. Ultrasonic vibration-assisted laser engineered net shaping of Inconel 718 parts: effects of ultrasonic frequency on microstructural and mechanical properties. J Mater Process Technol 2020;276:116395. https://doi.org/10.1016/j.jmatprotec.2019.116395.
[41] Tilita G-A, Chen W, Leung CKL, Kwan CCF, Ma RLW, Yuen MMF. Influence of ultrasonic excitation on the mechanical characteristics of SLM 304L stainless steel. Procedia Eng 2017;216:18–27. https://doi.org/10.1016/j.proeng.2018.02.084.
[42] Maskery I, Parry LA, Padrão D, Hague RJM, Ashcroft IA. FLatt Pack: a research-focussed lattice design program. Addit Manuf 2022;49:102510. https://doi.org/10.1016/j.addma.2021.102510.
[43] Gibson LJ, Ashby MF. Cellular solids: structure and properties. second ed. Cambridge: Cambridge University Press; 1997. https://doi.org/10.1017/CBO9781139878326.
[44] Maskery I, Sturm L, Aremu AO, Panesar A, Williams CB, Tuck CJ, Wildman RD, Ashcroft IA, Hague RJM. Insights into the mechanical properties of several triply periodic minimal surface lattice structures made by polymer additive manufacturing. Polymer 2018;152:62–71. https://doi.org/10.1016/j.polymer.2017.11.049.
[45] Yin H, Zheng X, Wen G, Zhang C, Wu Z. Design optimization of a novel bio-inspired 3D porous structure for crashworthiness. Compos Struct 2021;255:112897. https://doi.org/10.1016/j.compstruct.2020.112897.
[46] ISO 13314:2011(en), Mechanical testing of metals — Ductility testing — Compression test for porous and cellular metals, (n.d.). https://www.iso.org/obp/ui/#iso:std:iso:13314:ed-1:v1:en (accessed July 29, 2023).
[47] Zhang C, Zheng H, Yang L, Li Y, Jin J, Cao W, Yan C, Shi Y. Mechanical responses of sheet-based gyroid-type triply periodic minimal surface lattice structures fabricated using selective laser melting. Mater Des 2022;214:110407. https://doi.org/10.1016/j.matdes.2022.110407.
[48] Van Bael S, Kerckhofs G, Moesen M, Pyka G, Schrooten J, Kruth JP. Micro-CT-based improvement of geometrical and mechanical controllability of selective laser melted Ti6Al4V porous structures. Materials Science and Engineering: A 2011;528:7423–31. https://doi.org/10.1016/j.msea.2011.06.045.
[49] Fan X, Tang Q, Feng Q, Ma S, Song J, Jin M, Guo F, Jin P. Design, mechanical properties and energy absorption capability of graded-thickness triply periodic minimal surface structures fabricated by selective laser melting. Int J Mech Sci 2021;204:106586. https://doi.org/10.1016/j.ijmecsci.2021.106586.
[50] Zhang D, Zhang P, Liu Z, Feng Z, Wang C, Guo Y. Thermofluid field of molten pool and its effects during selective laser melting (SLM) of Inconel 718 alloy. Addit Manuf 2018;21:567–78. https://doi.org/10.1016/j.addma.2018.03.031.
[51] Chi J, Song H, Shao H, Zhou Y, Zheng Q, Lu N, Starostenkov MD, Dong G, Bi J, Tan C. Inhibiting of softening behavior in AA2219 laser welded joints. Materials Science and Engineering: A 2025;924:147742. https://doi.org/10.1016/j.msea.2024.147742.
[52] Song H, Zhao C, Bai H, Ren X, Shao H, Chi J, Dong G, Bi J, Tan C. Investigation of grain boundary segregation evolution and corrosion behavior in 7050 aluminum alloy under oscillating laser melting. J Alloys Compd 2025;1010:177524. https://doi.org/10.1016/j.jallcom.2024.177524.
[53] Wen S, Du Y, Tan J, Liu Y, Zhou P, Long J, Kaptay G. A new model for thermal conductivity of "continuous matrix/dispersed and separated 3D-particles" type composite materials and its application to WC-M (M = Co, Ag) systems. J Mater Sci Technol 2022;97:123–33. https://doi.org/10.1016/j.jmst.2021.04.036.
[54] Jung J-G, Ahn T-Y, Cho Y-H, Kim S-H, Lee J-M. Synergistic effect of ultrasonic melt treatment and fast cooling on the refinement of primary Si in a hypereutectic Al–Si alloy. Acta Mater 2018;144:31–40. https://doi.org/10.1016/j.actamat.2017.10.039.
[55] Richter B, Hocker SJA, Frankforter EL, Tayon WA, Glaessgen EH. Influence of ultrasonic excitation on the melt pool and microstructure characteristics of Ti-6Al-4V at powder bed fusion additive manufacturing solidification velocities. Addit Manuf 2024;89:104228. https://doi.org/10.1016/j.addma.2024.104228.
[56] Wang X, Muñiz-Lerma JA, Attarian Shandiz M, Sanchez-Mata O, Brochu M. Crystallographic-orientation-dependent tensile behaviours of stainless steel 316L fabricated by laser powder bed fusion. Materials Science and Engineering: A 2019;766:138395. https://doi.org/10.1016/j.msea.2019.138395.
[57] Liu W, Liu C, Wang Y, Zhang H, Li J, Lu Y, Xiong L, Ni H. Tailoring the microstructural and mechanical properties of 316L stainless steel manufactured by laser powder bed fusion. J Mater Res Technol 2023;25:7389–405. https://doi.org/10.1016/j.jmrt.2023.07.158.
[58] Moyle M, Ledermueller C, Zou Z, Primig S, Haghdadi N. Multi-scale characterisation of microstructure and texture of 316L stainless steel manufactured by laser powder bed fusion. Mater Char 2022;184:111663. https://doi.org/10.1016/j.matchar.2021.111663.
[59] Wang M, Song B, Wei Q, Shi Y. Improved mechanical properties of AlSi7Mg/nano-SiCp composites fabricated by selective laser melting. J Alloys Compd 2019;810:151926. https://doi.org/10.1016/j.jallcom.2019.151926.
[60] Gao C, Wu W, Shi J, Xiao Z, Akbarzadeh AH. Simultaneous enhancement of strength, ductility, and hardness of TiN/AlSi10Mg nanocomposites via selective laser melting. Addit Manuf 2020;34:101378. https://doi.org/10.1016/j.addma.2020.101378.
[61] Li W, Yang Y, Liu J, Zhou Y, Li M, Wen S, Wei Q, Yan C, Shi Y. Enhanced nanohardness and new insights into texture evolution and phase transformation of TiAl/TiB2 in-situ metal matrix composites prepared via selective laser melting. Acta Mater 2017;136:90–104. https://doi.org/10.1016/j.actamat.2017.07.003.
[62] Hong Y, Zhou C, Zheng Y, Zhang L, Zheng J. The cellular boundary with high density of dislocations governed the strengthening mechanism in selective laser melted 316L stainless steel. Materials Science and Engineering: A 2021;799:140279. https://doi.org/10.1016/j.msea.2020.140279.
[63] Zhao M, Ji B, Zhang DZ, Li H, Zhou H. Design and mechanical performances of a novel functionally graded sheet-based lattice structure. Addit Manuf 2022;52:102676. https://doi.org/10.1016/j.addma.2022.102676.
[64] Murr LE, Esquivel EV, Quinones SA, Gaytan SM, Lopez MI, Martinez EY, Medina F, Hernandez DH, Martinez E, Martinez JL, Stafford SW, Brown DK, Hoppe T, Meyers W, Lindhe U, Wicker RB. Microstructures and mechanical properties of electron beam-rapid manufactured Ti–6Al–4V biomedical prototypes compared to wrought Ti–6Al–4V. Mater Char 2009;60:96–105. https://doi.org/10.1016/j.matchar.2008.07.006.
[65] Zhao M, Zhang DZ, Liu F, Li Z, Ma Z, Ren Z. Mechanical and energy absorption characteristics of additively manufactured functionally graded sheet lattice structures with minimal surfaces. Int J Mech Sci 2020;167:105262. https://doi.org/10.1016/j.ijmecsci.2019.105262.
[66] Choy SY, Sun C-N, Leong KF, Wei J. Compressive properties of functionally graded lattice structures manufactured by selective laser melting. Mater Des 2017;131:112–20. https://doi.org/10.1016/j.matdes.2017.06.006.
[67] AlMahri S, Santiago R, Lee D-W, Ramos H, Alabdouli H, Alteneiji M, Guan Z, Cantwell W, Alves M. Evaluation of the dynamic response of triply periodic minimal surfaces subjected to high strain-rate compression. Addit Manuf 2021;46:102220. https://doi.org/10.1016/j.addma.2021.102220.
[68] Li X, Xiao L, Song W. Compressive behavior of selective laser melting printed Gyroid structures under dynamic loading. Addit Manuf 2021;46:102054. https://doi.org/10.1016/j.addma.2021.102054.
[69] Zhong T, He K, Li H, Yang L. Mechanical properties of lightweight 316L stainless steel lattice structures fabricated by selective laser melting. Mater Des 2019;181:108076. https://doi.org/10.1016/j.matdes.2019.108076.
[70] Xiao L, Feng G, Li S, Mu K, Qin Q, Song W. Mechanical characterization of additively-manufactured metallic lattice structures with hollow struts under static and dynamic loadings. Int J Impact Eng 2022;169:104333. https://doi.org/10.1016/j.ijimpeng.2022.104333.